The VenSpec-U spectrometer onboard EnVision: sensitivity studies

Lucile Conan, Emmanuel Marcq, Benjamin Lustrement, Nicolas Rouanet, Léna Parc, Sandrine Bertran, Séverine Robert, Jörn Helbert, Giulia Alemanno

To cite this version:

Lucile Conan, Emmanuel Marcq, Benjamin Lustrement, Nicolas Rouanet, Léna Parc, et al.. The VenSpec-U spectrometer onboard EnVision: sensitivity studies. Infrared Remote Sensing and Instrumentation XXXII. Proceedings SPIE 13144, Aug 2024, San Diego, United States. 43 p., 10.1117/12.3027500 . insu-04733439

HAL Id: insu-04733439
https://insu.hal.science/insu-04733439v1

Submitted on 15 Oct 2024

The VenSpec-U Spectrometer onboard EnVision mission: a Sensitivity Study

Lucile Conan[a], Emmanuel Marcq[a], Benjamin Lustrement[a], Nicolas Rouanet[a], Léna Parc[a], Sandrine Bertran[b], Jörn Helbert[d], Ann Carine Vandaele[c], Giulia Alemanno[d]

[a]*LATMOS/IPSL, UVSQ Université Paris-Saclay, Sorbonne Université, CNRS, Guyancourt, France*
[b]*Hensoldt Space Consulting, Guyancourt, France*
[c]*Royal Belgian Institute for Space Aeronomy (BIRA-IASB), Brussels, Belgium*
[d]*DLR Institute of Planetary Research, Berlin, Germany*

Abstract

The dual-channel UV spectrometer VenSpec-U onboard ESA's next mission to Venus, EnVision, will study the upper layer of the atmosphere located above the clouds. It aims to characterise the chemical composition, with a focus on the sulphured gases (SO_2 and SO) and the identification of the unknown UV absorber, and will also monitor the dynamical processes such as gravity waves and convection cells. In this article, we are interested in knowing how the instrumental design allows to comply with requirements arising from these scientific objectives. This study is based on the radiative transfer model (RTM) developed for SPICAV/Venus-Express data analysis, that is used to retrieve of atmospheric features from radiance factor spectra, which will be derived from VenSpec-U's measurements of Venus' radiance. We will then study the sensitivity of the model to various error sources: random errors or biases. For the first ones, we assess the impacts of the Signal-to-Noise Ratio on the uncertainties of the inverse RTM outputs, in order to check that the required uncertainties are achieved for the main science goals. Limits in terms of SNR can also be defined in order to ensure the compliance with the specifications. We then present the approach implemented for the characterisation of systematic errors: the Effective Spectral Radiometric Accuracy (ESRA) requirement is used to estimate the impact of a bias on the accuracy of the retrieved science products based on the spectral characteristics of the biased spectra. After identifying some bias sources that could occur in VenSpec-U' case, combinations are considered in order to study potential compensations and estimate allowable envelopes of residual error levels for each kind.

Keywords: radiative transfer, instrumentation, modelling

---

1. Introduction

UV observations have been used to study Venus' mesosphere for more than five decades. Several instruments have performed measurements using UV imaging and spectroscopy, in order to investigate the structure and composition of this part of the atmosphere, located above the upper limit of the cloud layer around 65 to 70 km of altitude. These observations allowed to identify sulphured species as minor components, like sulphur-dioxide (SO_2) or sulphur-monoxide (SO) that were first detected with the space telescope IUE (International Ultraviolet Explorer) (Barker, 1979; Na et al., 1990). The UV spectrometer UVS onboard Pioneer Venus Orbiter then monitored the long-term variations in the SO_2 abundance above the clouds, and showed a significant secular decrease over a decade (Esposito et al., 1979, 1988). Using data from following missions, including the more recent Venus-Express, other species such as ozone (O_3) and chlorine based components like chlorine monoxide (ClO) (Mills and Allen, 2007; Zhang et al., 2012; Marcq et al., 2019) were detected among minor components. The imaging spectrometer STIS onboard the Hubble Space Telescope also performed high-resolution measurements of SO_2 and SO and provided an estimation of the SO/SO_2 abundance ratio, ranging between 7% and 18% (Jessup et al., 2015). In addition, spectral analysis revealed the presence of a constituant showing a broad absorption band centred around 365 nm (Heyden et al., 1959). Correlations have been noticed between the presence of this unidentified UV absorber and the cloud-top altitude, as well as temporal anti-correlation with the SO_2 abundance above the clouds, which could imply conversion processes between these species and a sulphured-bearing UV absorber (Marcq et al., 2020). The upper atmosphere also hosts interesting dynamical features, both on large and smaller scales. UV imagers VMC/Venus-Express (Markiewicz et al., 2007) and UVI/Akatsuki (Yamazaki et al., 2018) have shown latitudinal contrasts at a planetary scale, and smaller patterns similar to gravity waves and convection cells, at a scale ranging from 3 to 20 km (Titov et al., 2008; Peralta et al., 2008; Titov et al., 2012; Piccialli et al., 2014).

Despite the most recent data obtained thanks to these missions, interrogations remain regarding the processes involving the sulphured trace gases and the UV absorber. Their sources, conversion mechanisms, spatial and temporal variability, and implication in the sulphur cycle are not yet fully understood (Vandaele et al., 2017; Marcq et al., 2018). Surface observations revealing volcanic structures (Head et al., 1991) have brought up the hypothesis of a connection with internal activity. This highlights the need for investigating the characteristics and causes of this internal activity, as well as its relationship with atmospheric composition. Currently active volcanism could indeed explain long-term variations in the concentration of the sulphur species observed at cloud top (Esposito, 1984; Marcq et al., 2013) through destabilization of the static stability profile and enhanced mixing between the lower atmosphere (sulphur-rich) and the upper atmosphere (sulphur-poor). In order to investigate these unresolved questions (among others), three missions are planned for the early 2030s (Widemann et al., 2023): VERITAS (Smrekar et al., 2022) and DaVinci (Garvin et al., 2022) from NASA. Onboard the latter, the spectrometer CUVIS and one of the VISOR cameras will perform UV studies of the clouds. Finally, the ESA mission EnVision (Ghail et al., 2017) will investigate the couplings between the surface of Venus, its atmosphere and internal activity. It will also seek information on the history and evolution of the planet. To that end, the payload includes a synthetic aperture radar (VenSAR, provided by NASA) for surface mapping, a subsurface radar sounder, a radio science experiment to study gravimetric and atmospheric properties, and the VenSpec suite, composed of three spectrometers (Helbert et al., 2019). The suite aims to study the surface of Venus and different layers of the atmosphere, using the thermal IR imager VenSpec-M to observe the surface and characterise its composition and mineralogy, and the high resolution IR spectrometer VenSpec-H to study the composition of the atmosphere below the clouds. Lastly, VenSpec-U (Marcq et al., 2021) will operate in the UV range and focus on the upper part of the atmosphere, above the cloud layer.

As VenSpec-U aims to further the knowledge about the composition and dynamical properties of the upper atmosphere, its characteristics must allow for an improvement of the science return compared to previous UV investigations. A good understanding of the performances of the instrument is therefore needed to improve the interpretation of the provided data and the relevance of the retrieved scientific products. Requirements have been defined in the early phases of the development and expected accuracy levels have been set regarding the main science objectives (Marcq et al., 2021). It is now important to know how the current instrumental design complies with these specifications, and what are its impacts on the performances. This article therefore summarises the approach used to assess the management of errors, of whether random or systematic nature. Section 2 presents the instrumental concept of VenSpec-U and its scientific objectives, before describing the radiative transfer model that aims to simulate the observations of Venus to be provided by the instrument. Section 3 summarises the main performance-related requirements, as well as the simulation cases used for the performances assessments studies presented in the following sections. After describing the approach related to random errors in Section 4, the implemented method regarding systematic errors management is explained in Section 5, including examples of specific cases of bias likely to be encountered by the instrument.

2. The VeSUV experiment

VenSpec-U, also called VeSUV (standing for "Venus Spectroscopy in UV"), is one of the three spectrometers of the VenSpec suite onboard the EnVision spacecraft. This section gives an overview of the instrumental concept, which was previously detailed by Marcq et al. (2021).

2.1. Instrument description

The main scientific goals of VenSpec-U are to measure the column densities of SO_2 and SO and follow their spatial and temporal variability, which will also provide an estimate of the column abundance ratio SO/SO_2. Another objective is related to the monitoring of the UV absorber as well as constraining its spectral characteristics. Lastly, it will provide observations of dynamical patterns on scales larger than $\sim 10\,\mathrm{km}$, such as the convection cells and gravity waves structures.

To do so, VenSpec-U will measure the sunlight backscattered by the atmosphere on the dayside of Venus. Observations will be carried out from a low polar orbit, between 150 and 500 km of altitude, using a pushbroom strategy in a nadir or near-nadir (emission angle $< 15°$) geometry. They shall be repeated on 4 consecutive orbits, every 16 orbits. The overlap of the observed scenes allows to distinguish the causes of the observed variability, whether it originates from surface or purely atmospheric phenomena, as the latter would be carried away by the zonal superrotation between two consecutive orbits. Radiance factor spectra are therefore processed using the spectral radiance from Venus measured by the instrument, and the prior knowledge of the Solar Spectral Irradiance (SSI). The radiance factor β is defined as follows:

$$\beta(\lambda) = \frac{\pi\,\mathrm{sr} \cdot I(\lambda)}{F_{\odot}(\lambda)}$$

where $I(\lambda)$ refers to the observed spectral intensity from Venus and $F_{\odot}(\lambda)$ is the solar spectral irradiance.

The spectrometer will perform those measurements using two channels. The first one, called "Low Resolution" (LR), operates in the 190-380 nm band with a comparatively low spectral resolution of 2 nm. This channel is dedicated to measuring SO_2 through its absorption bands centered around 215 nm and 283 nm. The extended wavelength range also enables the observation of the short-wavelength part of the absorption band of the UV absorber centered around 365 nm. Its relatively low spectral resolution allows in return for a high spatial resolution, allowing the observation of dynamical phenomena ranging from 5 to 10 km in scale. The second channel, called "High Resolution" (HR), has a narrower wavelength range, from 205 nm to 235 nm, with a spectral resolution of 0.3 nm. As the high spectral resolution enables the identification of individual absorption lines, the SO and SO_2 contributions can be distinguished and the SO/SO_2 abundance ratio can be determined robustly. For photometric reasons, the spatial resolution is comparatively coarser, ranging from 12 to 24 km. Each channel will be composed of an entrance baffle, a two-lenses objective including a stop diaphragm, a slit leading to a short-pass filter to cut out the wavelengths higher than the limit of each channel's range, and a spherical holographic grating for the spectral dispersion of the images. Both channels will use the same CMOS backsideilluminated detector, coupled to a Peltier cooler in order to limit the dark current. A specific area of the detector is dedicated to each spectrum, for which the narrow axis of the slit gives the spectral dimension, and the long axis of the slit results in the spatial dimension associated to both channels' common 20° instantaneous field of view. The orbital scrolling then provides the second spatial dimension. Distinct integration time, spectral and spatial binning, and stacking configurations will be implemented for each channel to optimise the acquisitions. The optical layout and simulated spectra are presented in Fig. 1.

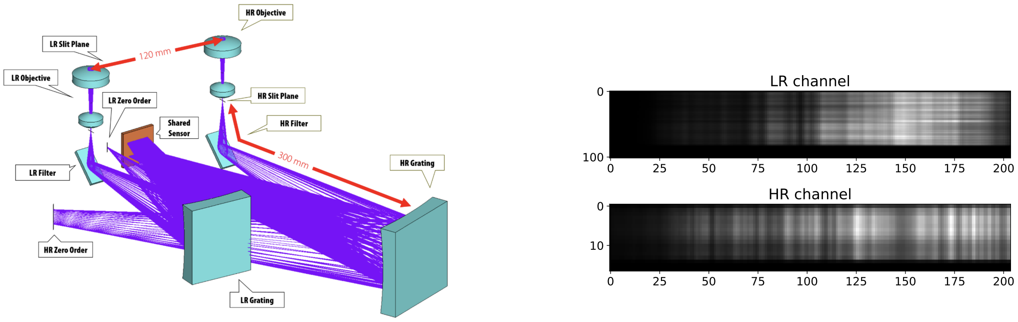

Figure 1: VenSpec-U optical design (left) and shared detector with dedicated areas for LR and HR channels (right)

2.2. *Forward radiative transfer model*

In order to simulate the instrument's output and produce synthetic radiance factors, a Radiative Transfer Model (RTM) is used. The model has been implemented for the data analysis of SPICAV/Venus-Express (Marcq et al., 2019, 2020), and has been updated to encompass the wavelength range of VenSpec-U. It was thus extended to the larger wavelengths, from 190-320 nm up to 190-380 nm.

The atmospheric model considers altitudes ranging from 50 to 110 km, divided into 2 km thick layers. The VIRA-2 profile (Moroz and Zasova, 1997) is used for the temperature, and the density is derived assuming hydrostatic equilibrium. The relevant quantities (optical thickness, single scattering albedo, phase function) derived from the atmospheric components are then computed for each layer.

The influence of the main gaseous components of the atmosphere, CO_2 and N_2, appear mostly through Rayleigh scattering and absorption for CO_2 (at wavelengths shorter than 220 nm). A uniform distribution with respect to the altitude is considered, with volumetric fractions of respectively 0.965 and 0.035. The other considered gases are SO_2, SO and OCS. The abundances of variable species SO and SO_2 are controlled using their mixing ratios at an altitude of 70 km from which the columns densities are deduced, assuming exponential decreases of the abundances with increasing altitudes. The associated absorption opacities are then determined using the absorption cross-section of each species (Fig. 2) as in Marcq et al. (2019) for wavelengths shorter than 320 nm. The cross-section profiles of the minor species like OCS have been extrapolated between 320 nm and 380 nm as a constant equal to the value at 320 nm, since their influence is negligible at higher wavelengths, whereas data from Bogumil et al. (2003) covering wavelengths from 239 nm to 395 nm have been used for the extension of the SO_2 cross-section, and SO cross-sections have been updated using data from Heays et al. (2023). CO_2,

SO_2 and SO cross-sections are temperature-dependent and are interpolated assuming a linear relation between the logarithm of the cross-sections and the inverse of the temperature.

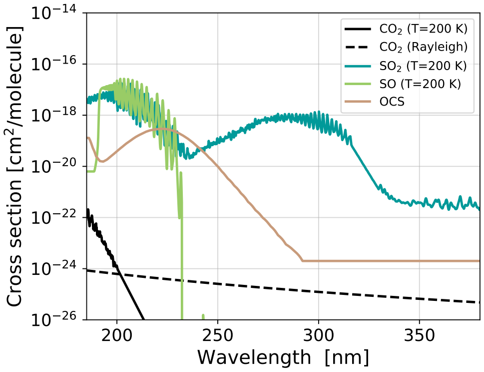

Figure 2: Absorption cross-section of gaseous species extended up to 380 nm

The absorption due to the droplets from the upper clouds and haze is then taken into account. These aerosols are considered as spherical particles, so that the Mie scattering theory can be applied. A bimodal distribution with a log-normal probability density function is assumed (Luginin et al., 2016). Each mode has specific properties, including the effective radius of the droplets, the effective variance, as well as a complex refractive index: an imaginary part is added to the refractive index, in order to model the UV absorber. While this imaginary part is assumed constant for the mode 2, it parameterizes the influence of the UV absorber embedded within the smaller mode 1 particles. For the latter, a wavelength-dependent spectrum was defined using data from Pérez-Hoyos et al. (2018) and Lee et al. (2022). It was then adjusted to fit both SPICAV spectra toward the shorter wavelengths, for which the index was defined as $m_i(\lambda) = m_i(\lambda = 250\,\mathrm{nm}) \cdot e^{\frac{\lambda - 250\,\mathrm{nm}}{40\,\mathrm{nm}}}$ and controlled using $m_i(\lambda = 250\,\mathrm{nm})$, and the spectrum from Pérez-Hoyos et al. (2018) around the upper wavelengths (Fig. 3). It resulted in the following modified Lorentzian function, whose amplitude is adjusted through $m_i(\lambda = 350\,\mathrm{nm})$:

$$m_i(\lambda) = \frac{m_i(\lambda = 350\,\mathrm{nm})}{1 + \left|\frac{\lambda - 350\,\mathrm{nm}}{51.84\,\mathrm{nm}}\right|^{2.7}}$$

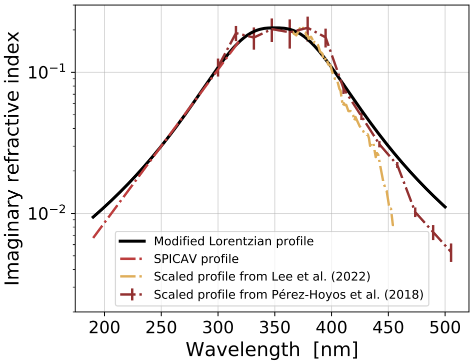

Figure 3: Imaginary refractive index profile of mode 1 particles

The extinction cross-section, single scattering albedo and Legendre polynomial coefficients of the particle's phase functions are then determined for each mode according to the corresponding columns densities, which allows to derive the associated opacity. Once the contributions to the radiative budget of each layer are determined, the pseudo-spherical code SPS-DISORT (Stamnes et al., 1988) provides radiance factors from the resulting brightness at the top of atmosphere, for each wavelength of interest and a given observation geometry.

The input parameters of the forward model are the key parameters that will be monitored by VenSpec-U. Some of these parameters relate to the chemical composition of the atmosphere, such as the SO_2 mixing ratio at an altitude of 70 km (noted `qSO2`), the abundance ratio SO/SO_2 (noted `rSO`), and the imaginary part of the refractive index at a wavelength of 250 nm used to represent the influence of the UV absorber (noted `img`). The cloud top altitude (defined as the altitude for which the opacity due to the aerosols at a wavelength of 250 nm is equal to one) is constrained through the `Z2` parameter. Finally, the observation geometry is represented by three angles: the Solar Zenith Angle (SZA), the emission angle and the phase angle. In a nadir observation geometry, the emission angle is close to zero, and the phase angle equivalent to the SZA. With VenSpec-U's operation conditions, the emission angle could be ranging up to 20°, and the performances of the instrument are considered for SZA under 70°. Influence of these parameters upon synthetic radiance factors are shown in Fig. 4.

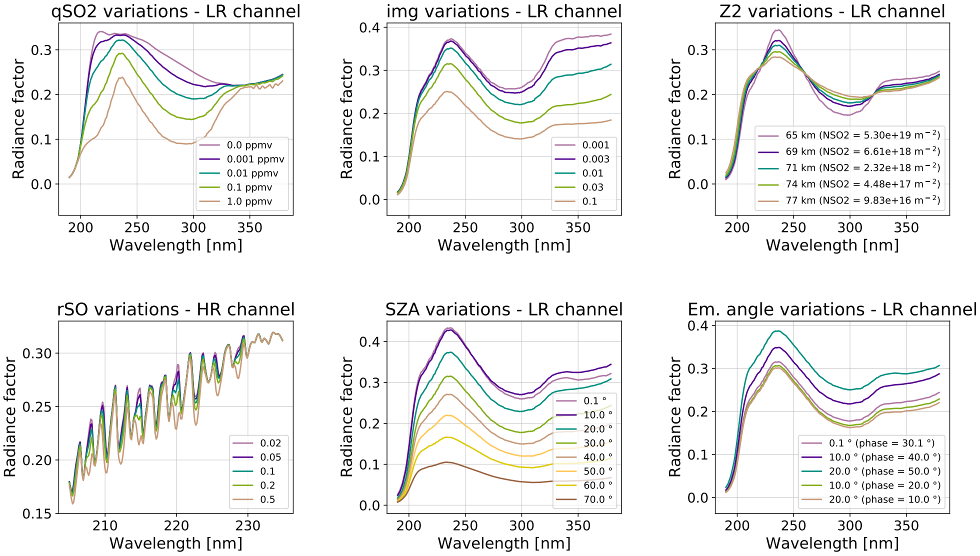

Figure 4: Synthetic radiance factors with variation of the input parameters of the FRTM. Initial parameters correspond to the Nominal observation scenario summarised in Table 2

2.3. Inverse radiative transfer model

As described in the previous section, the radiative transfer model can be used in its direct form to generate radiance factors from a set of parameters describing the atmosphere and the observation geometry. The RTM can also be used to deduce these quantities from a radiance factor spectrum, using a fitting procedure based on a Levenberg-Marquardt method (Newville et al., 2020). The following function (of spectral index j) is minimised with respect to the L2 norm by the optimisation algorithm:

$$r_j = \frac{\beta_{j,\mathrm{noised}} - \beta_{j,\mathrm{fit}}}{e_j} \quad \text{with} \quad e_j = \frac{\beta_{j,\mathrm{true}}}{\mathrm{SNR}_j}$$

It corresponds to the difference between the undisturbed theoretical spectrum and the spectrum generated with the parameters resulting from the fit, weighted by a random error on the radiance factor. The amplitude of this random component depends on the wavelength and corresponds to the ratio between the initial radiance factor level and the Signal-to-Noise Ratio (SNR). This results in favouring longer wavelengths to find the most adequate parameters, as random errors are smaller on this portion of the spectrum.

The fitted parameters differ between the two simulated channels of VenSpec-U, depending on which quantities will be retrieved. Both channels will provide information about the UV absorber and SO_2 abundance. Therefore, the following parameters will be fitted on both LR and HR radiance factors: `qSO2` and `img`. `Z2` will be retrieved thanks to the LR channel only, whereas `rSO` only through the HR channel.

3. Performance assessments

3.1. Performance-related requirements

In order to translate the scientific objectives into constraints applicable to the measurements and define requirements related to the radiance factor estimation, a set of instrumental parameters has been defined in the early phases of the project (Marcq et al., 2021). This instrumental set-point represents a compromise between spectral resolution, noise and biases allocations, that allows to reach the goals in term of retrievals accuracy. These requirements are presented for the main scientific objectives in Table 1, where accuracy requirements are expressed using a logarithmic scale so that: $\ln(X_{measured}) - \frac{e}{100} < \ln(X_{true}) < \ln(X_{measured}) + \frac{e}{100}$, with e the relative accuracy expressed in percentage.

	Requirements			
Scientific objectives	SNR (normalised at 220 nm)	Random precision	Effective Spectral Radiometric Accuracy	Absolute Radiometric Accuracy (at 365 nm)
Measure the SO_2 columns density above the clouds	≥ 200	$< 20\%$	< 50 %	-
Measure the SO/SO_2 columns density ratio	≥ 100	$< 25\%$	< 100 %	-
Perform long-term monitoring of the UV absorber and clouds	≥ 100	-	-	< 10 %

Table 1: Main performance-related requirements

The presence of noise on the signal leads to uncertainties associated with the retrieved atmospheric characteristics by the RTM. A precision constraint has then been set for the main science goals to ensure that these uncertainties, corresponding to the expected variance of the measurements, would be sufficiently small for the data analysis. The verification of the "random precision" requirement will therefore be presented in Section 4. On the other hand, the "Effective Spectral Radiometric Accuracy" requirement (Copernicus Sentinels 4 & 5 MRTD, ESA, 2017) is referring to the impact of systematic errors on the accuracy of the retrievals. It allows to combine effects of biases, studied independently, with the sensitivity of the model estimated through a Gain matrix representing the linearised inverse RTM. The formalism, as well as a the influence of multiple bias sources, will be explored in more details in Section 5.

3.2. Simulation cases

In order to characterise the achievable performances of the instrument for a representative set of operation conditions, several Venus observation scenarios are defined. Three typical simulation cases are considered to define a radiometric envelope for the measurements provided by VenSpec-U depending on the observed scenes. Variable assumptions between these scenarios are relative to intrinsic parameters of the atmosphere such as the abundances of SO_2, SO, and the UV absorber, as well as the SZA to describe the observation conditions. Common parameters of these simulation cases include the nadir viewing configuration, resulting in a zero emission angle, and a fixed cloud-top altitude (which does not affect the modeled radiance as much as the other parameters). Table 2 summarises the parameters associated to each case, and the corresponding radiance factor spectra are shown in Fig. 5.

The “Nominal” scenario corresponds to an average case, with atmospheric conditions allowing a correct signal level and for which the absorption bands of the atmospheric compounds are well defined. This case therefore represents the performances expected for the majority of the instrument’s observations.

The “MaxPerf” case allows to study the upper bounds of the instrument’s performances, and designates situations where all optimal radiometric conditions are met. The illumination is maximal and the signal level is high due to the atmospheric composition, for which lower concentrations of absorbing species are considered. On the contrary, the “MinPerf” scenario corresponds to a degraded radiometric performance case. For this latter, an atmosphere with a high absorbers content is considered, which contributes to a lower radiance emitted by Venus, and consequently a lower signal received by the instrument. In addition, illumination conditions are set at the SZA limit for which the targeted performances are guaranteed. This allows to estimate the behavior of the instrument for a non-optimal case and thus assessing its minimal performances. These scenarios are also used for the assessment of radiometric performances, for which other instrumental parameters such as detector temperature or components efficiencies are considered.

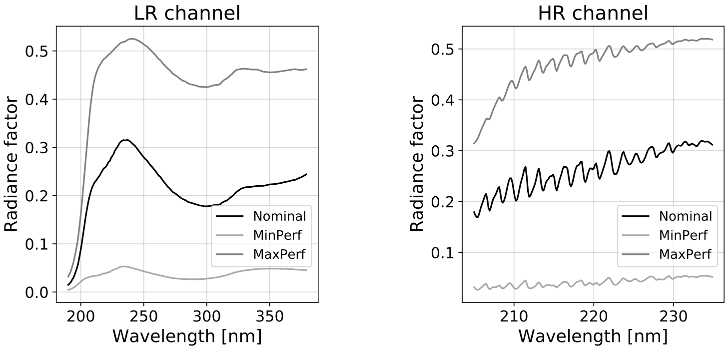

Figure 5: Synthetic radiance factors corresponding to the three simulation cases for LR (left) and HR (right) channels

RTM parameter		MinPerf	Nominal	MaxPerf
SO_2 mixing ratio at 70 km (ppm)	`qSO2`	0.5	0.02	0.001
UV absorber imaginary refractive index at 250 nm	`img`	0.2	0.03	0.003
Cloud-top altitude control point (km)	`Z2`	70	70	70
SO/SO_2 abundances ratio	`rSO`	0.25	0.1	0.05
Solar Zenith Angle (°)	`SZA`	70	30	0
Emission angle (°)		0	0	0
Phase angle (°)		70	30	0

Table 2: FRTM parameters of the simulations cases

The sensitivity studies presented in the following sections, regarding both random and systematic errors, will therefore be carried out for these three cases in order to compare the effects of each type of uncertainty.

4. Random errors

This section focuses on the sensitivity of the inverse RTM to the random errors that generates noise on the radiance factor spectra. As the signal-to-noise ratio is used as an optimisation parameter in the Levenberg-Marquardt algorithm, which results in an increased reliance on certain portions of the spectrum, variations of the SNR level and spectral shape can influence the uncertainties associated to the retrieved parameters.

The fitting is therefore performed after introducing noise on a synthetic radiance factor spectrum using various perturbations of the reference SNR spectrum, presented in Fig. 6 and derived from instrumental design. Two types of perturbations can be considered (Fig. 7): a multiplicative factor, which allows to keep the same spectral shape by affecting all wavelengths uniformly ; or a “gamma correction” in order to maintain the maximal SNR level but altering the spectral shape by affecting the shorter and longer wavelengths differently:

$$\mathrm{SNR}(\lambda) = \mathrm{SNR}_{\mathrm{ref}}(\lambda) \cdot f \quad \text{or} \quad \mathrm{SNR} = \max_{\lambda}(\mathrm{SNR}_{\mathrm{ref}}) \cdot \left(\frac{\mathrm{SNR}_{\mathrm{ref}}(\lambda)}{\max_{\lambda}(\mathrm{SNR}_{\mathrm{ref}})} \right)^{\gamma}$$

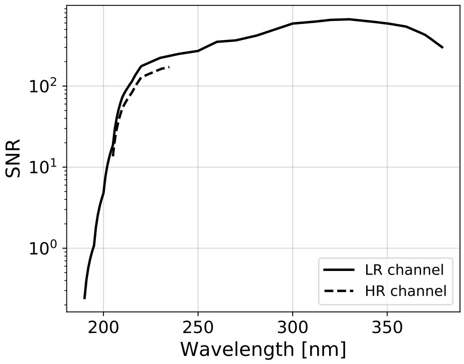

Figure 6: Reference Signal-to-Noise Ratio for LR and HR channels

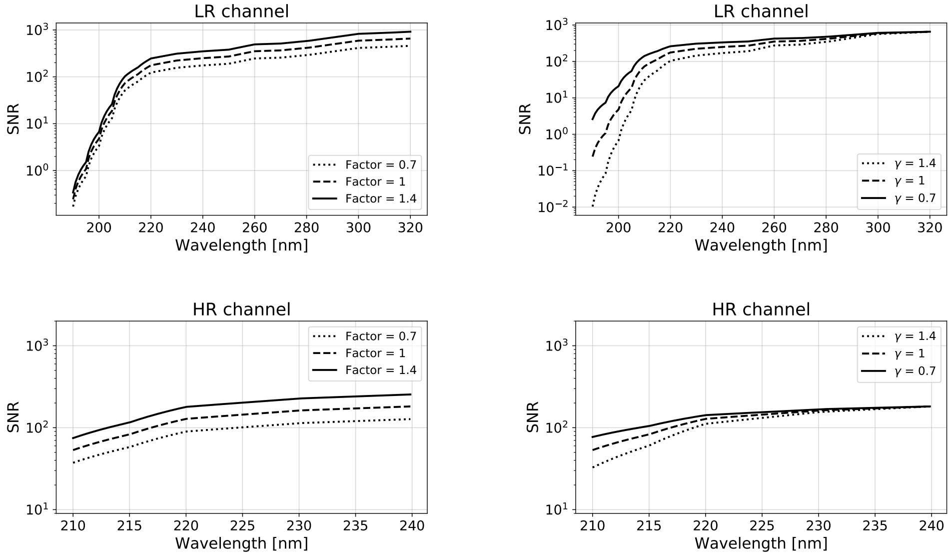

Figure 7: Modified Signal-to-Noise Ratio with multiplicative factor (left) or gamma exponent (right), for LR (top row) and HR (bottom row) channels

The resulting variations of the relative uncertainty associated to each retrieved parameter are shown in Fig. 8 for the global shift in the SNR level by the multiplicative factor, and in Fig. 9 for the distortion of the SNR spectrum by the gamma exponent. The relative uncertainty is defined as the ratio of the standard error associated to the estimated parameter, and the prescribed RTM parameter.

The required relative uncertainties associated to the retrieval of the SO_2 and SO abundances, namely 20% and 25%, are achieved in most cases. An exception occurs however for the `rSO` retrieval in the MaxPerf scenario. This

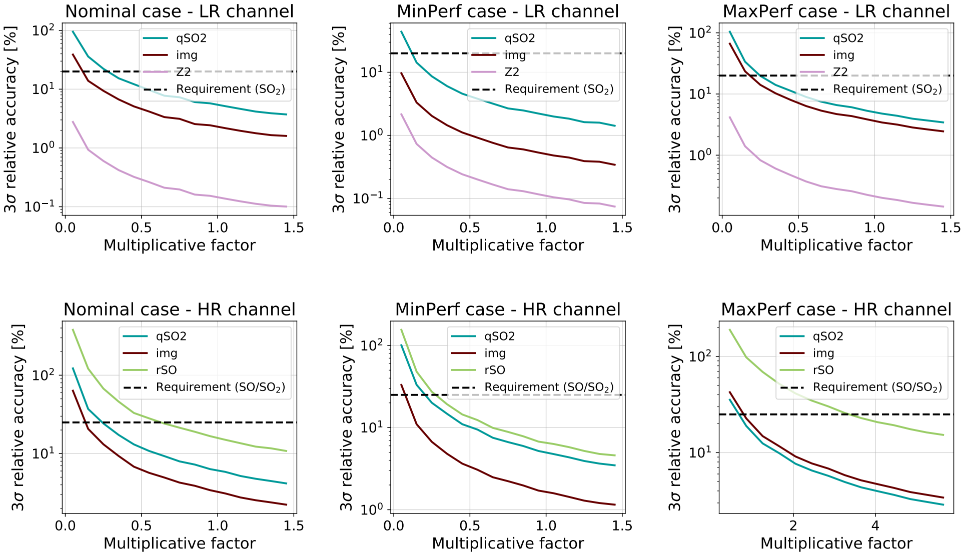

Figure 8: Relative uncertainty of the fitted parameters for the LR (top row) and HR (bottom row) channels, for the three scenarios : Nominal (left column), MinPerf (center) and MaxPerf (right column)

case indeed consider a low SO_2/SO abundances ratio, which makes the absorption lines hard to distinguish from the noise. The resulting uncertainties are bigger than the requirement for most tested SNR levels or shapes, and an increase of the SNR by a multiplicative factor of at least 3 would be needed to reach the desired precision. If the maximal value of the SNR is however unchanged like it is the case with the gamma correction, uncertainties on the rSO retrieval would remain above 50%. It therefore implies a sensitivity threshold around 0.025 ppb for the detection of sulphur monoxide. Ignoring the combination of the MaxPerf case and HR channel, the most constraining

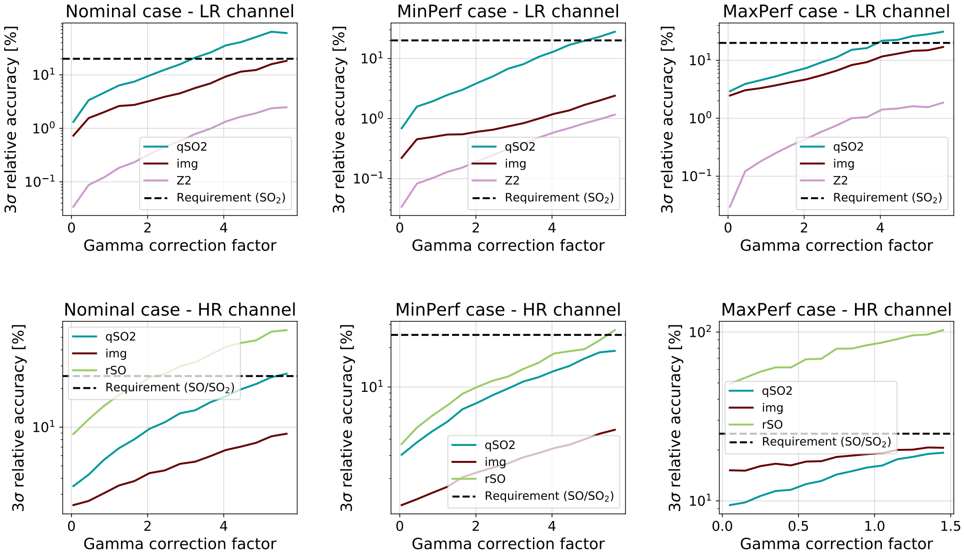

Figure 9: Relative uncertainty of the fitted parameters for the LR (top row) and HR (bottom row) channels, for the three scenarios : Nominal (left column), MinPerf (center) and MaxPerf (right column)

limits are encountered in the Nominal scenario for both LR and HR channels, regarding respectively the `qSO2` and `rSO` precision requirements. Envelopes defining boundaries in terms of SNR can then be determined in order to ensure that the required precisions are reached (Fig. 10). Fig. 11 shows typical noised spectra for these SNR limits, and the corresponding precision for other fitted parameters can be estimated. With the LR channel, the biggest uncertainties are found in the MaxPerf case for both the cloud-top altitude (`Z2`) and the imaginary refractive index modeling the UV absorber (`img`), which are retrieved with relative uncertainties around 0.67 km and 12.9% respectively. For the HR channel, the uncertainty on the imaginary refractive index is ranging up to 5.17%, while it is lower than 10.2% for the estimation of the SO_2 mixing ratio (`qSO2`). These uncertainties are smaller than in the previous study from Marcq et al. (2021), where the SNR was estimated using the inverse of the square root of a synthetic radiance, and has since been determined more precisely by taking instrumental parameters into account.

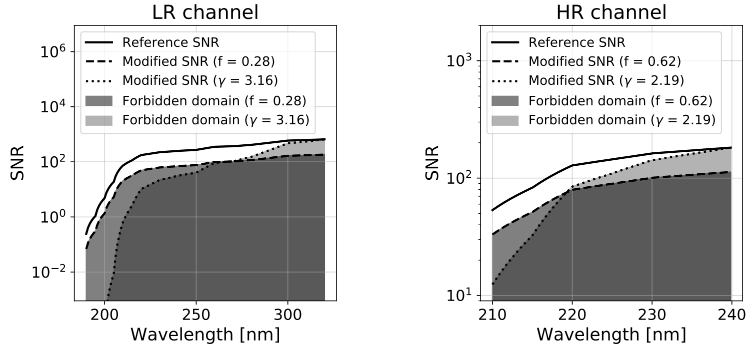

Figure 10: Limitation of SNR domains for LR and HR channels

The fitting is here restricted to the 190-320 nm spectral range, corresponding to the range of SPICAV-UV data which has been validated to derive these observable parameters (Marcq et al., 2020). The radiance factors produced for wavelengths between 320 and 380 nm are indeed based on extrapolations. Moreover, as SNR is better for longer wavelengths, performing this sensitivity study on the whole wavelength range of VenSpec-U's LR channel would result in underestimating the impact of random errors on the uncertainties. The precision of the retrievals shall therefore improve compared to the above given values when the full wavelength range will be considered, provided no

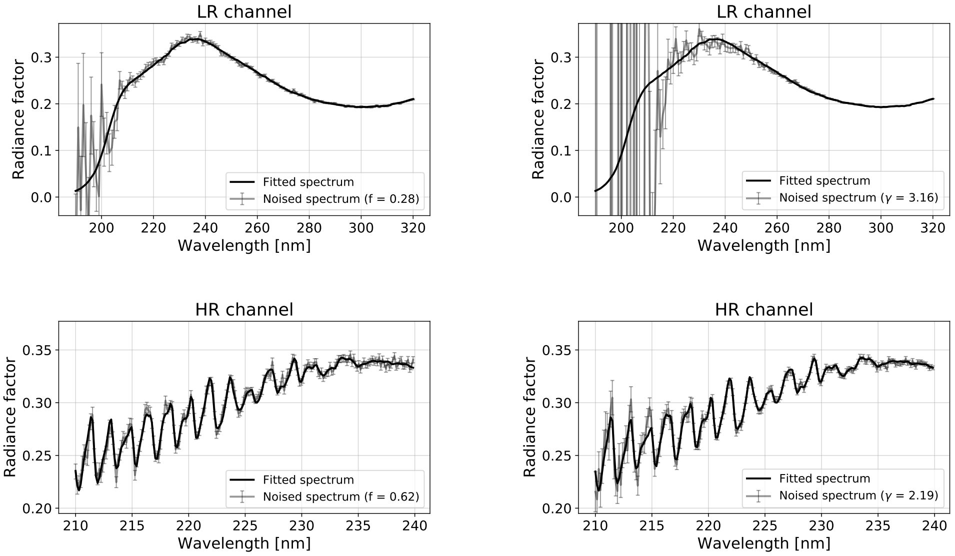

Figure 11: Fitted and noised spectra with lowest multiplicative factor (left) or largest gamma exponent (right) fullfilling the requirement, for LR (top row) and HR (bottom row) channels

extra variable parameters are required to fit the 320-380 nm interval (e.g. relating to the UV absorber spectrum).

5. Systematic errors

The following section is focused on the characterisation of systematic errors, also referred to as biases, and the assessment of their impact on the radiance factor spectra provided by the instrument. It addresses more specifically the accuracy of the retrievals of science data, which corresponds to the relative difference between the retrieved and actual atmospheric characteristics, such as sulphured gases abundances, cloud-top altitude and UV absorber characteristics. The biases can have various impacts on the signal measured by the instrument, and can lead to an amplification, attenuation or deformation of the resulting radiance factor spectra. Depending on the type of bias, these effects can either induce a global perturbation of the signal or be strongly wavelength-dependent. The potential causes of bias can be identified from the knowledge of the instrumental design, and its operation conditions. Consequently, the effects on the signal can be anticipated through models and specific studies, in order to predict the type and magnitude of the impact that will occur according to each bias source. A correction can therefore be applied, to extract the useful spectra from the biased signal. However, as the spectrum of the biases' effects can't be perfectly known, a residual bias is still contained in the output signal. This study refers more specifically to the accuracy loss due to this remaining bias.

5.1. Effective Spectral Radiometric Accuracy (ESRA)

The wavelength dependence of these induced deformations of the radiance factor spectra dictates the severity of the resulting error made on the estimation of the atmospheric characteristics. The precision is especially degraded if the biases induce a distortion of the same spectral shape as a theoretical unbiased spectrum. Indeed, if the perturbations show similarities with the spectra of the observed scene, the discrepancy between the retrieval of the atmospheric characteristics using the RTM and their actual values will be increased. The fitting algorithm will not be able to distinguish the source of the spectral feature, whether it is due to the expected cause, here the absorption by atmospheric components, or comes from an external effect like a potential bias. In order to account for the precision loss induced on the retrievals of the atmospheric parameters by these spectral similarities between the useful and biased signals, the Effective Spectral Radiometric Accuracy (ESRA) for the i-th retrieved parameter is used. As introduced in section 3.1, this requirement was defined to ensure that the effect of possible measurement biases would not affect the retrieved values as to jeopardize the scientific objectives of the instrument. The global ESRA envelope for the SO_2 and SO abundance retrievals, which are respectively 50% and 100% on a relative scale, should be achieved for 90% of the observations. It is expressed as follows:

$$\mathrm{ESRA}_i = \Delta\lambda \cdot \sum_j G_{ij} \cdot (\beta_{j,\mathrm{measured}} - \beta_{j,\mathrm{true}})$$

where β_j stand for the radiance factor measured for the j-th spectral index, $\Delta\lambda$ the wavelength step, and G_{ij} the so-called *gain matrix.* The estimation of the ESRA will then allow to determine the sensitivity of the instrument to a certain type of bias. The contribution of each type of bias must however be estimated to verify that the specification is met, and identify the most potentially concerning biases.

This requirement formulation is based on a gain matrices formalism. The interest of this approach comes from the fact that all causes of bias can be treated independently and in a similar way. The biases are considered as small perturbations, so that the variations of the inverse RTM can be linearised as in the formula defining ESRA. As a result, the radiance factor deformations can be examined wavelength by wavelength, instead of examining the effect of a global deformation of the spectra. Any spectral shape of biased spectra can then be considered. Once the potential sources of bias are identified, their impact on the ESRA are assessed independently. For each relevant wavelength depending on the instrument's channel, the resulting bias on the atmospheric parameters are identified, and combined into a gain vector associated to a specific parameter of the RTM.

5.2. Computation of gain matrices

Two methods for the determination of the gain matrices have been implemented and are presented in the following sections. Both methods give similar results, but the second one reduces the computation time significantly, from about a week to a dozen minutes on a standard desktop computer.

5.2.1. RTM inversion

The first method implemented for the gain matrix computation relies on the inverse RTM. By introducing perturbations on a spectrum generated with the forward model with a specific set of parameters and by using the inverse RTM to find equivalent parameters associated to this deformed spectrum, the errors made on the retrieval of the parameters is deduced from the difference between the initial and the fitted quantities. The uncertainties related to the effects of spectral distortions on the results of the fitting algorithm can then be estimated. However, the determination of the precision loss caused by a bias is only valid for the tested deformation spectra. As the objective of the implemented method is to determine a gain vector, the perturbations must target a single wavelength, which allows to estimate the resulting deviation on the parameters for this specific wavelength.

The process detailed hereafter is repeated for all the wavelengths independently. A radiance factor spectrum is first generated with the direct RTM from a set of parameters corresponding to a typical observation case. A single-wavelength disturbance of varying magnitude $\delta\beta_j = \delta\beta(\lambda_j)$ is then introduced, and then a random error vector, following the prescribed SNR vs. wavelength function, is added over the entire spectrum. This locally distorted and noised spectrum then becomes the input data of the inverse RTM. The element of the gain vector corresponds to the proportionality coefficient of the relative error between the output of the inverse RTM and the input of the forward RTM, and the relative amplitude of the disturbance introduced on the radiance factor spectrum (Fig. 12):

$$G_{ij}(p) = \left(\frac{\delta p_i / p_{i,\mathrm{ref}}}{\delta\beta_j} \right)_{|\beta_{i \neq j}}$$

This implies an assumption of linearity, which is valid if the introduced perturbations are small. The gain matrix results in the stacking of the gain vectors, that refers to a parameter of the RTM (namely `qSO2`, `img`, `rSO` or `Z2`).

For each channel, the gain vectors are computed for the wavelengths in the spectral range with a step corresponding to the spectral resolution. It results in wavelengths ranging from 190 to 380 nm with a 2 nm step for the LR channel, while the wavelengths are between 205 and 235 nm, with a 0.3 nm step for the HR channel. The results are shown in Fig. 13. The noisy aspect observed for wavelengths above 320 nm is due to numerical instabilities rather than expected spectral features, which is also indicated by the size of the error bars.

The major drawback of this method is the long computation time of the

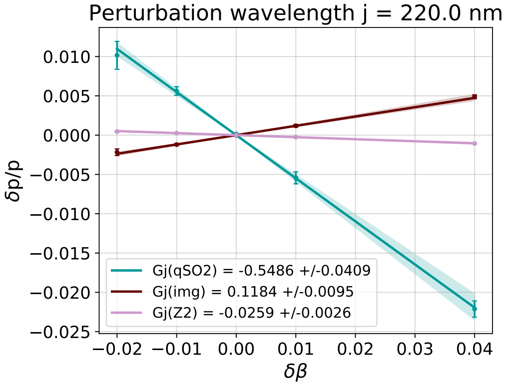

Figure 12: Gain vectors elements for each fitted parameter at 220 nm, for the LR channel and Nominal scenario

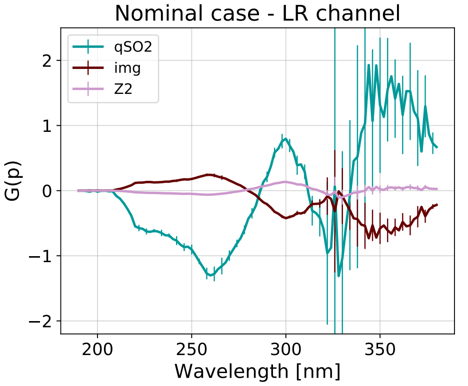

Figure 13: Gain vector of each fitted parameter for the LR channel and Nominal scenario

gain vectors, as the calculation involves the fitting algorithm and is made for one wavelength at a time. This process however allows the estimation of error bars associated to the gain matrix elements.

5.2.2. Jacobian matrix inversion

In order to optimise the process and reduce the computation time, a new approach has been implemented. This method consists in expressing the linearised RTM model in a matrix form. The gain matrix then corresponds to the matrix inverse of the RTM. As the iterative fitting algorithm isn't involved in this process, the computation time is significantly reduced. This approach is valid in the linearity domain of the RTM, as it is based on the conversion through the matrices of perturbations on input parameters into perturbations on the radiance factors. It therefore implies small perturbations, as residual biases are expected to be.

The matrix associated with the forward RTM, the Jacobian matrix (noted A hereafter), is first computed. It consists in the partial derivatives with respect to each variable parameter involved in the generation of the radiance factors. It is defined so that:

$$\delta\beta_j = \sum_{k=1}^{M} \left(\frac{\partial \beta_j}{\partial ln(p_k)} \right) \delta ln(p_k) = \sum_{k=1}^{M} A_{jk} \cdot \frac{\delta p_k}{p_k} \quad \text{or} \quad \begin{pmatrix} \delta\beta_1 \\ \vdots \\ \delta\beta_N \end{pmatrix} = A \cdot \begin{pmatrix} \frac{\delta p_1}{p_1} \\ \vdots \\ \frac{\delta p_M}{p_M} \end{pmatrix}$$

It allows to convert a deviation on the input parameters Δp_k into a deviation on the resulting radiance factor spectrum for each wavelength $\Delta\beta_j$. This matrix has for dimension the number of variable input parameters of the model (M), as well as the number of points at which the radiance factors are estimated (N), which corresponds to the wavelengths (usually, $N \gg M$). Each column of this matrix is a gain vector related to one of the input parameters of the forward RTM. They are computed one by one using the forward RTM, before being stacked into the Jacobian matrix. To do so, several radiance factor spectra are generated from a set of parameters, each with a slight variation of a single parameter. The Jacobian matrix elements are retrieved from this set of spectra by a linear fit between the deviation on the radiance factor resulting from the introduced variation of the input parameter (Fig. 14).

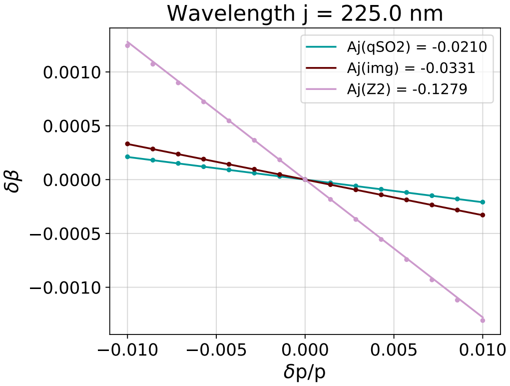

Figure 14: Jacobian matrix elements for each fitted parameter at 225 nm, for the LR channel and Nominal scenario

The inverse RTM can be expressed in the same way with the gain matrix (noted "G"), which allows to convert a deviation in radiance factor $\delta\beta_j$ into a deviation in atmospheric parameters δp_k:

$$\frac{\delta p_k}{p_k} = \sum_j G_{kj} \cdot \delta\beta_j \quad \text{or} \quad \begin{pmatrix} \frac{\delta p_1}{p_1} \\ \vdots \\ \frac{\delta p_M}{p_M} \end{pmatrix} = G \cdot \begin{pmatrix} \delta\beta_1 \\ \vdots \\ \delta\beta_N \end{pmatrix}$$

It is then simply computed by inverting the Jacobian matrix, using a Moore-Penrose pseudo-inverse as the latter is not square. In order to stay consistent with the method detailed in the previous section, the impact of the wavelength dependence of the random errors on the fitting strategy must also be considered. Indeed, the minimised cost function of the inverse RTM is favouring the wavelengths where the SNR is better, in order to estimate the parameters allowing the best coincidence between the initial and fitted spectra. This effect is introduced in the expression of the pseudo-inverse of the Jacobian matrix, as a square diagonal matrix S which represents the variance of the measurements (Sierk et al., 2014). Similarly to the Levenberg-Marquardt algorithm, the Moore-Penrose pseudo-inversion estimates the best solution for the inverse matrix using least square optimisation. The variance matrix allows to modify the contribution of each point to the cost function, by attributing a weight on the wavelengths depending on the SNR. The gain matrix is then computed as follows:

$$G = \frac{1}{\Delta\lambda} \cdot \left(A^T \cdot S^{-1} \cdot A\right)^{-1} \cdot \left(A^T \cdot S^{-1}\right) \quad \text{with} \quad S_{ij} = \delta_i^j \left(\frac{\beta_j}{SNR_j}\right)^2 - \ell \cdot L_{ij}$$

where L is a regularization matrix defined hereafter.

The matrices of the various simulation cases are plotted in Fig. 16. It shows the wavelength-dependence of the sensitivity to bias for each parameter retrieved by the fitting algorithm, and how a variation in the radiance factor level can lead to an over- or under-estimation of this parameter, depending on the sign of the gain vector. Correlations between the gain vectors can also be observed, especially between the `qSO2` and `img` parameters, whose gain vectors have similar variations but inverted signs. Indeed, a lower radiance factor can be caused either by a deepening of the SO_2 absorption bands with higher SO_2 abundance, or by a global darkening of the spectrum with an increase of the UV absorber influence through the `img` parameter. The fitting algorithm can then compensate the effect of a parameter by giving an opposite behaviour to another, leading to higher sensitivity to biases on these portions of the spectrum. Some intersections of the gain vectors are however close to zero, so the sensitivity to biases is consequently lower for all parameters simultaneously. These nodes can be found around similar wavelengths for the different simulation cases and could be used as control points.

Small instabilities on the Jacobian matrix are amplified in the inversion, which causes the gain vectors to appear noisy. As these fine spectral structures are not expected in the inversion's output (for the LR channel), the gain matrix is computed using a modified variance matrix defined as: $S - \ell \cdot L$, where the regularisation matrix L corresponding to the discrete second derivative operator is combined to the initial variance matrix and the smoothness is adjusted for each scenario through the coefficient ℓ (Fig. 15). This parameter is set for the Nominal, MinPerf, and MaxPerf cases to respectively 7e-7, 1e-8 and 2e-5.

$$L = \begin{pmatrix} -1 & 1 & 0 & \dots & 0 \\ 1 & -2 & 1 & \dots & 0 \\ \dots & \dots & \dots & \dots & \dots \\ 0 & \dots & 1 & -2 & 1 \\ 0 & \dots & 0 & 1 & -1 \end{pmatrix}$$

The sampling of the radiance factor spectra used to compute the Jacobian matrix elements can also influence the smoothness of the resulting gain vectors. The effect of the wavelength step of the radiance factor on the gain matrix aspect is shown in Fig. 17. The reference sampling value is considered

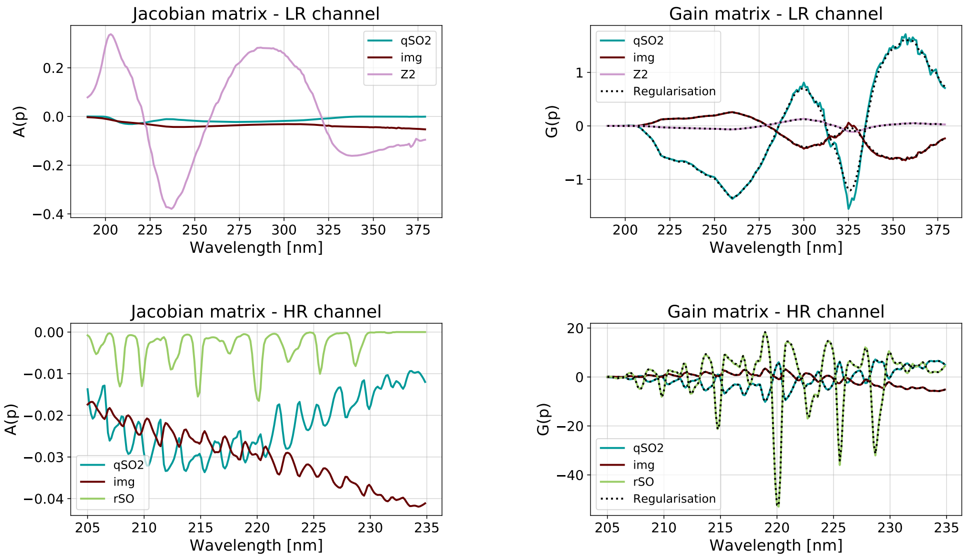

Figure 15: Jacobian and Gain matrices of the fitted parameters for the LR (top row) and HR (bottom row) channels, for the Nominal scenario. Préciser la valeur de ℓ ? Elle me semble d'ailleurs un peu faible ici, les variations selon une largeur typique moindre que la résolution spectrale de LR ne sont pas significatives...

as half of the channel spectral resolution, namely 1 nm for LR channel and 0.15 nm for HR channel. As the sampling is taken into account in the formulation of the gain matrix, through the $\Delta\lambda$ parameter, the amplitude of the resulting vectors is not modified. Small amplitude oscillations are however attenuated with an broader wavelength step, leading to a smoother aspect, but a wavelength step too wide can cause a loss of information, which suggests an optimal sampling of 5 nm for the LR channel's gain matrices computation. As HR matrices are less impacted by these perturbations, the sampling used for the computation can remain at 0.15 nm.

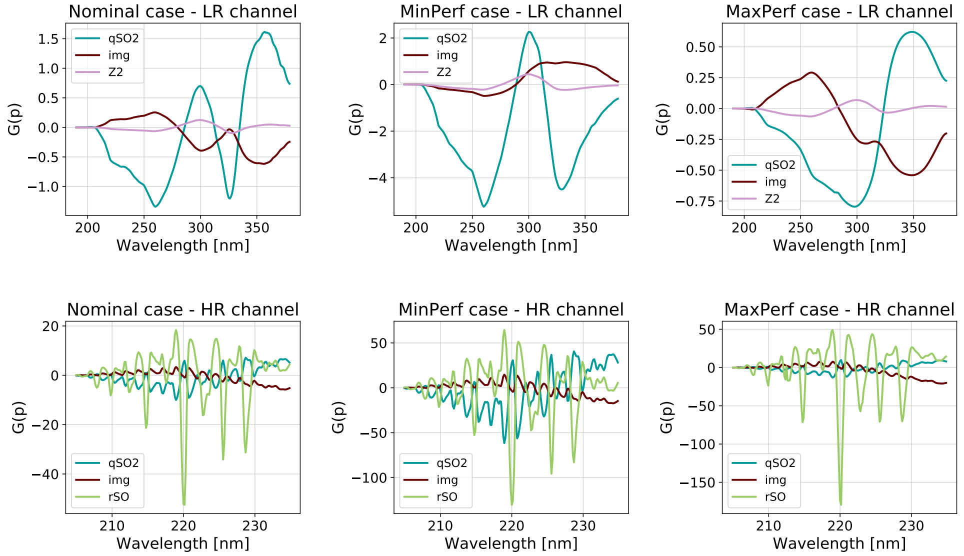

Figure 16: Gain vectors of the fitted parameters for the LR (top row) and HR (bottom row) channels, for the three scenarios: Nominal (left column), MinPerf (center) and MaxPerf (right column) La matrice MaxPerf qSO2 semble toujours souffrir de la discontinuité vers 280 nm que l'on a corrigée depuis...

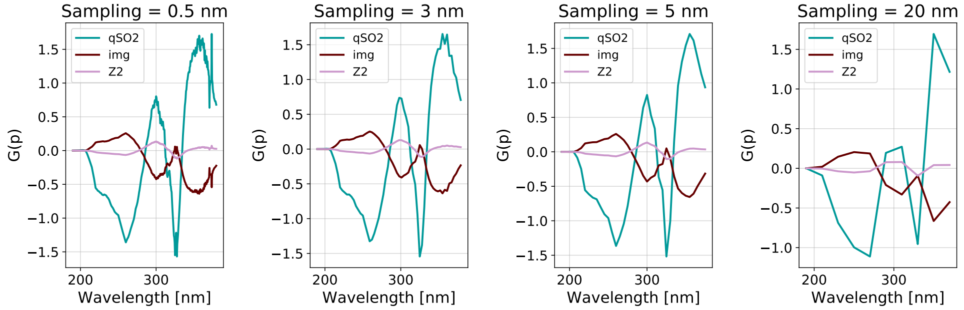

Figure 17: Non-regularised gain vectors of the fitted parameters with various samplings, for the LR channel and Nominal scenario Sont-ce des matrices régularisées ? Ça semble bruité à 0.5 nm

5.3. Bias characterisation approach

This section details the approach used for the allocation of error budgets, that aims to estimate a partition of the total ESRA specified envelope and the resulting allowable residual errors associated to each identified bias. As it is focused on the retrievals accuracy, this study relates to all biases that can affect the radiance factor, including direct perturbations of the measured signal, corresponding to Venus' radiance, or effects that occur in the radiance factor processing from the measurements. The severity of the biases are then determined using the gain matrices, by multiplying the deviation they induce on the radiance factor spectrum by the gain vector of the relevant parameter.

Two categories of biases are defined hereafter : "specific" or "generic" biases. The first category regroups the potential biases that have already been identified for VenSpec-U. The description of their effect on the signal or the derived radiance factor is therefore obtained from modeling of the instrumental pipeline. Four specific biases have been identified, and are described in sections 5.4.1 to 5.4.4. The second category represents general types of signal alterations, which are not linked to specific phenomena or instrumental effects and are therefore considered through simple analytical expressions. For instance, it corresponds to a constant offset or multiplicative factor on the measured radiance, which will be referred to as respectively "Additive" or "Multiplicative" biases in the following sections. Any effect introducing such perturbation of the radiance factor aims to be characterised in more details in the further development of the instrument and will ultimately be rather considered as a specific bias. However, the contribution of generic biases in the analysis allows to account for the biases whose effects on the signal have not yet been precisely formulated. They are therefore acting as placeholder biases.

5.4. Known specific biases

5.4.1. Straylight

One of the sources of bias that shall be encountered by VenSpec-U is the straylight. It refers to the light that doesn't follow the nominal path in the instrument, and results in adding signal to unexpected locations on the detector, which induces a perturbation of the shape or level of the radiance factor spectrum if not properly corrected. Straylight can come from external sources, such as the reflection of the Sun on the spacecraft, but it can also be generated inside the instrument by reflection on internal surfaces or scattering by various optical elements. However, external straylight is limited by entrance baffles, which prevent most of the unwanted external light to enter the instrument's field of view, and an internal baffle limits the overlapping between the channels' areas on the detector.

Studies have then been carried out by a contractor (Sophia Engineering) in order to characterise the impacts of the potential sources of straylight on the output signal. These studies have shown that the main straylight contributors in the collection subsystem are the lenses, mainly through scattering due to roughness and contamination, as well as intra-lens ghosts on a lower extend and mostly toward short wavelengths. In the spectrometer subsystem, straylight is mainly caused by in-band scattering of the filters and gratings, as other components like the detector window and mechanical parts have a comparatively negligible impact. A typical spectral shape of the relative level of the straylight with respect to the useful signal level is therefore shown in Fig. 18. A correction of the bias can be applied once this shape is known. As mentioned previously, the focus of this study relates to the residual error made on this correction. To that end, an uncorrected percentage of the residual error is considered, but the shape of the spectrum distortion remains the same.

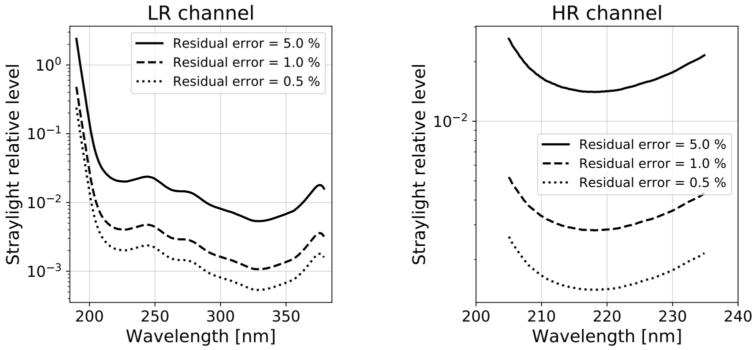

Figure 18: Residual straylight relative levels for LR (left) and HR (right) channels

It is then possible to deduce the deviation between a reference unbiased radiance factor spectrum and a spectrum containing a certain percentage of residual error (Fig. 19). The ESRA caused by straylight can then be determined, using the gain matrices.

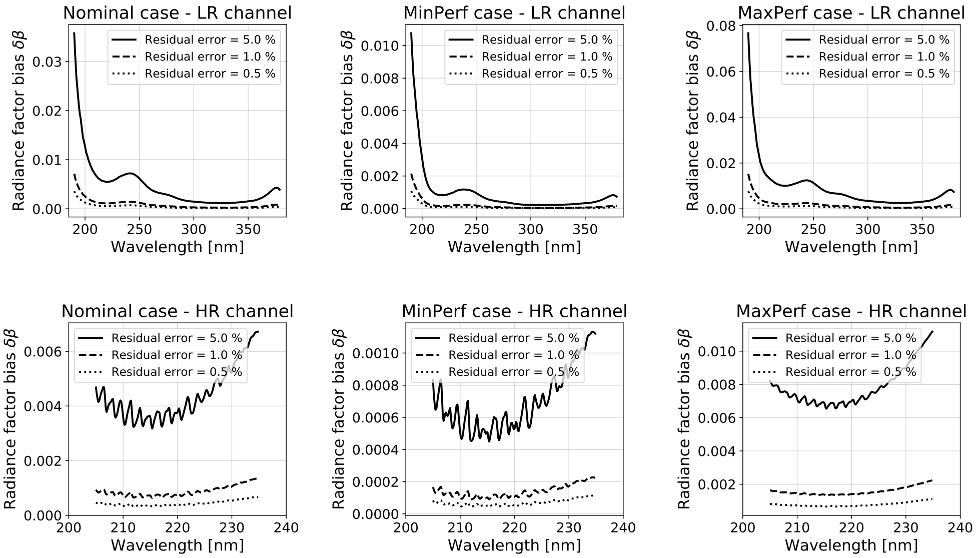

Figure 19: Radiance factor perturbation by a straylight-induced bias, for various residual error levels

5.4.2. Contamination

Another source of bias comes from the transmission loss caused by the progressive deposition of contaminants on the surface of optical elements. The induced signal attenuation is computed with absorption coefficients representing the behaviour of a combination of typical materials prone to release contaminants, using data from Muscari (1980). It results in a higher absorption toward shorter wavelengths, as shown is Fig. 20.

The spectral deformation, which is here also assumed proportional to the uncorrected bias, is presented in Fig. 21. Unlike the cases of bias detailed in the other sections, the transmission loss is computed from a thickness of the

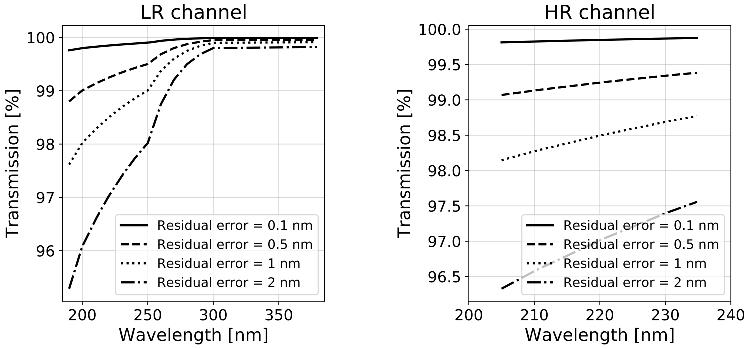

Figure 20: Residual transmission loss induced by contaminants for LR (left) and HR (right) channels

contaminant deposit, expressed in nanometers. Instead of a percentage with respect to a typical level, the residual errors used for the ESRA computation corresponds to the uncertainty associated to the estimation of this thickness during and in between in-flight calibrations.

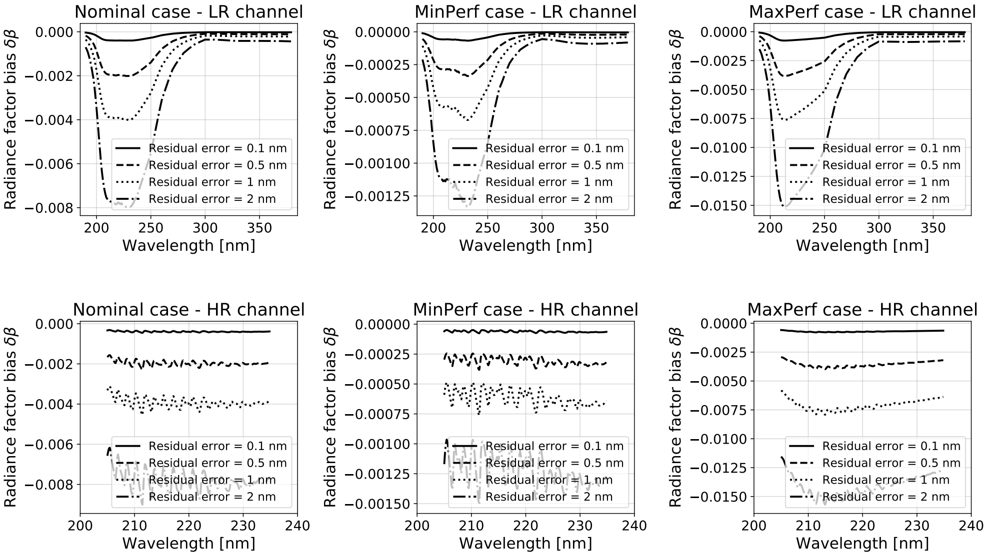

Figure 21: Radiance factor perturbation by a contamination-induced bias, for various residual error levels

5.4.3. Solar spectrum variability

The radiance factor provided by VenSpec-U is determined using the observed radiance of Venus and the Solar Spectral Irradiance (cf. Section 2.1). Knowledge of the solar spectrum is therefore essential to obtain a correct radiance factor estimation. It will ideally be provided by external monitoring of the solar spectra thanks to a dedicated instrument, similar to SOLAR/SOLSPEC (Bolsée et al., 2017) or SORCE/SOLSTICE (Mcclintock et al., 2000). However, it implies that such instruments are set up at the same time as EnVision. Extrapolation of these data and modelling of the solar activity could also be used to provide potentially missing information on the solar spectral irradiance, using information from previous solar cycles (Meftah et al., 2023).

The discrepancy between actual and assumed solar spectral irradiance is therefore considered as a source of bias, whose impact on the retrieval accuracy can be characterised using the gain matrices. To that end, the relative variability of the solar spectrum over the 11-year cycle is estimated (Fig. 22), considering the maximal deviation of the SSI between a solar maximum and a solar minimum, relatively to an averaged spectrum. Solar irradiance data are provided by the SOLAR/SOLSPEC instrument and covers the solar cycle 24 between 2008 and 2017. A spectrum from November 2014 is then used for the solar maximum, while a spectrum from August 2008 is used for the solar minimum.

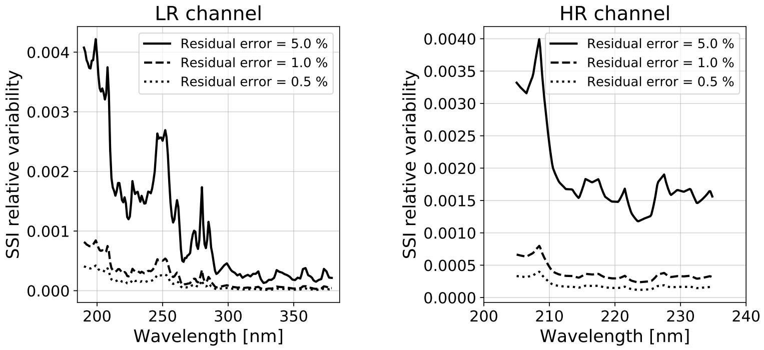

Figure 22: Residual relative variability of the solar spectrum over the 11-year cycle, for LR (left) and HR (right) channels

The impact on the radiance factor is then determined with respect to a typical radiance factor spectrum calculated with the averaged solar spectrum.

As a result, short wavelengths are more impacted by the uncertainties related to the variability, as shown in Fig. 23.

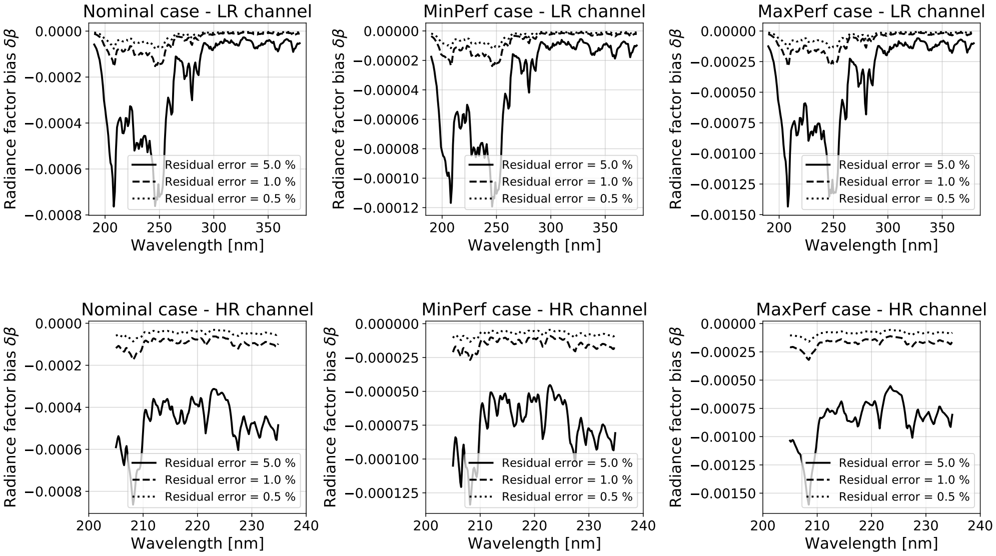

Figure 23: Radiance factor perturbation by a bias on the solar spectrum, for various residual error levels

5.4.4. Polarisation bias

The last bias detailled here is caused by the sensitivity of the instrument to the linear polarisation of the incoming light. An error is indeed introduced if the behaviour of the instrument differs depending on the properties of the source (the so-called *instrumental sensitivity*), as the current instrumental design does not involve any adjustments regarding this sensitivity. Two parameters must therefore be taken into account in order to estimate the impact of this type of bias on the radiance factor: the polarisation of the incoming radiance measured by the instrument, which corresponds to the solar light backscattered by the atmosphere of Venus, and the sensitivity of the instrument to polarisation.

A polarised radiative transfer model is used to compute the degree of polarisation of the observed scene (Fig. 24). It estimates the linear polarisation by giving the first two elements of the Stokes vector for a pure nadir viewing angle and varying SZA, for each of the reference atmospheric scenarii. The degree of polarisation is derived from the ratio of these two elements, and can be interpolated for various atmospheric conditions with similar inputs as the RTM presented in Section 2.2.

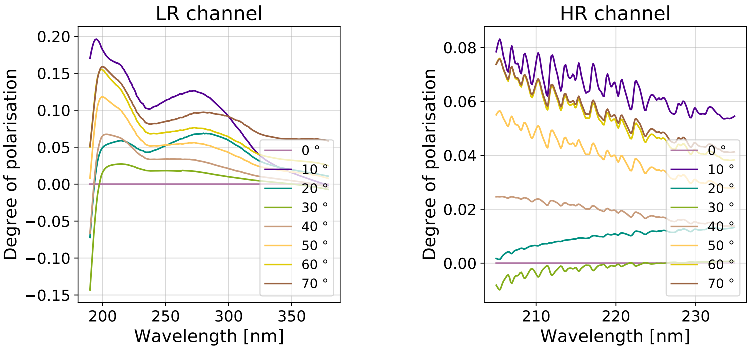

Figure 24: Venus linear degree of polarisation for various SZA, for LR (left) and HR (right) channels and MinPerf scenario

However, the simulation scenarios mentioned in the previous sections were defined from a radiometric point of view. They don't necessarily account for the corresponding situation in terms of polarisation, for which the best or worst cases can be reached for different observation configurations. The considered illumination angles are therefore modified, in order to have a more relevant estimation of the ESRA associated to the polarisation effects, while the other parameters of the simulation cases remain identical. The following SZA are then considered: 50° for the "Nominal" scenario, 30° for the "MaxPerf" scenario, and a 70° SZA is kept to represent the worst conditions in the "MinPerf" case.

The second parameter to take into account for the characterisation of the polarisation-induced bias is the sensitivity of the instrument (Fig. 25). It has first been estimated as step functions for broad wavelength ranges by considering the two types of components that have the most impact on polarisation, namely filters and gratings.

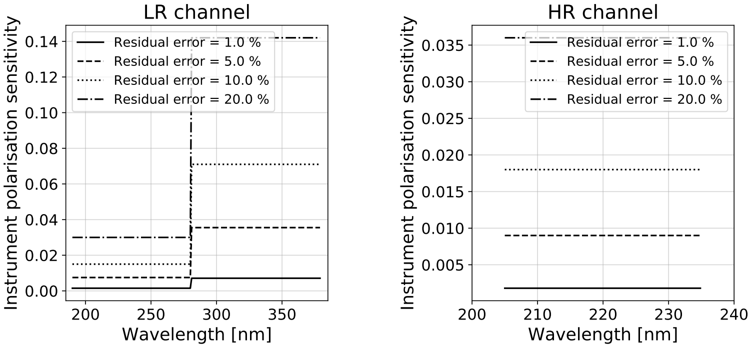

Figure 25: Residual polarisation sensitivity of the instrument, for LR (left) and HR (right) channels

The resulting relative error committed on the radiance factor is then derived from the relation:

$$\delta\beta(\lambda) = f(\lambda) \cdot W(\lambda) \cdot \cos(2\alpha)$$

where $f(\lambda)$ is the degree of polarisation of the source estimated with the previously introduced polarised radiative transfer model, $W(\lambda)$ is the sensitivity of the instrument, and α is the rotation angle of the axis of the source's polarisation around the instrument's line of sight. Given the range of observation geometries encountered by the instrument, it is a realistic assumption to consider a maximal absolute value of the cosine ($\alpha = 0^\circ \mod 90^\circ$). The perturbation of the radiance factor, shown in Fig. 26, and the associated ESRA can then be deduced.

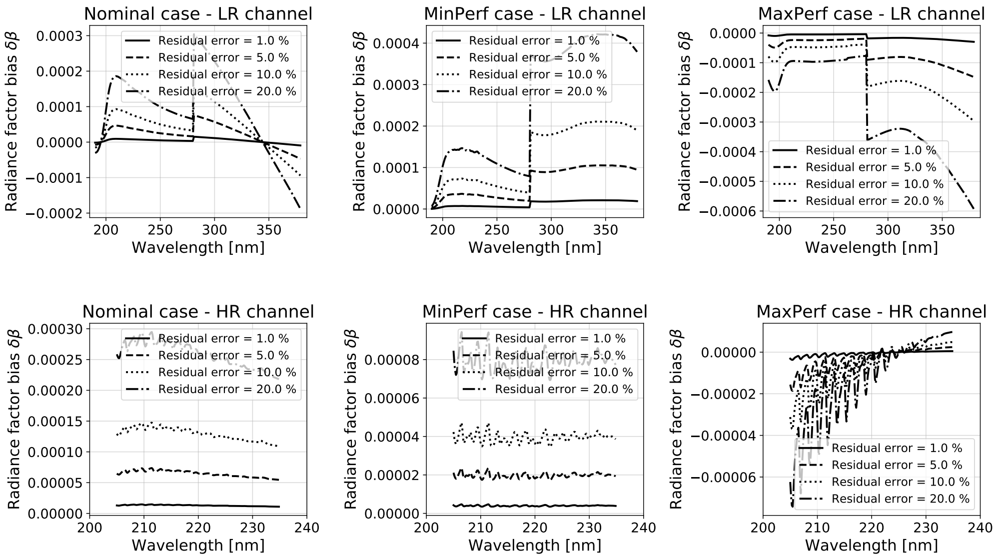

Figure 26: Radiance factor perturbation by a polarisation-induced bias for various residual error levels

5.5. ESRA budget allocations

5.5.1. Single source of bias

Various biases have been studied with respect to the ESRA requirement, that was defined to ensure a suitable accuracy of the scientific products derived from the radiance measurements. The impacts of residual errors have been assessed independently with a common method, and can now be compared in order to identify the biggest contributions to the global ESRA budget.

The severity of a bias results in a combination of two factors : the sensitivity to this source of error, given by the product of the induced radiance factor deformation and the gain matrices ; and the ability to correct it, which is yielded by the instrumental pipeline calibrations' efficiency. The sensitivity indicator is then defined for each bias as the inverse of the maximum allowable residual error (noted δx_0) that would be obtained if it was the only source of error and consuming the entire ESRA budget. The sensitivity factors of the four considered specific biases are shown in Fig. 27. Except for the contamination bias, which is computed for different values of contaminant deposit thickness, the yet identified biases are expressed as a percentage of a reference level. Consequently, a sensitivity factor below 1 corresponds to a maximum allowable residual error higher than the uncorrected bias. Straylight then appears overall as the most impactful source of error, whereas the polarisation-induced bias seems to be negligible. The HR channel also seems to be less sensitive to biases. Indeed, since the resolution allows to observe finer spectral structures, it is less likely for a bias' spectrum to be similar to these features, and then be mistaken for absorption lines.

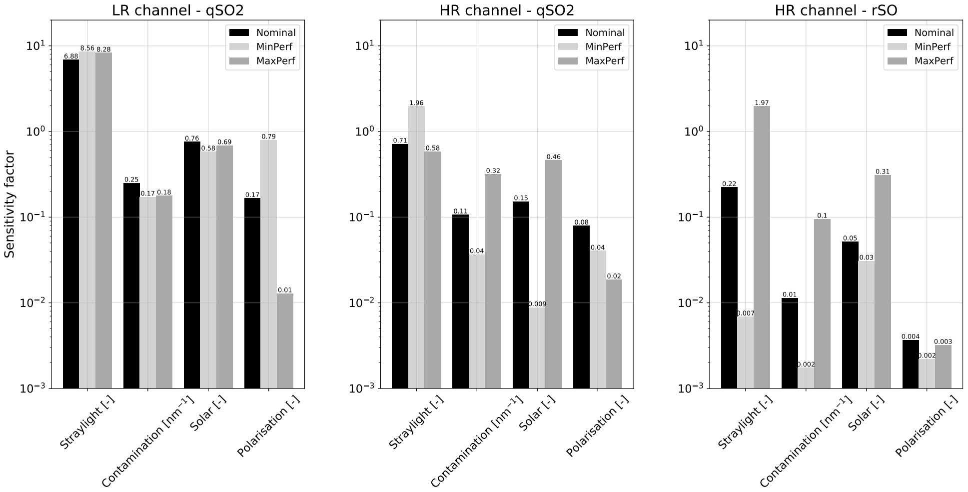

Figure 27: Sensitivity to specific biases, for LR (left) and HR (center and right) channels

5.5.2. Contribution of multiple sources of bias

Biases can however affect the radiance factor spectrum differently, whether their effects are opposite or located at different wavelengths. Some biases could then compensate each other to a certain extent, if the estimated residual errors weighted by their severity are equivalent. On the other hand, the combined effect of the same biases could result in an amplified error on the retrievals, if one is under-corrected while the other is over-corrected.

Once the effect of a bias is translated into a deformation of the radiance factor spectra, the associated ESRA can be determined via the gain matrices and the global error associated to a combination of biases is defined as the sum of the individual ESRA contributions. A statistical approach is then implemented, by randomly attributing a residual error level to each contributor with a uniform distribution, in order to define different envelopes: a domain allowing 100% compliance with the specification, on which a 10% margin is included to account for unforeseen biases, and a broader domain with 90% compliance. To enable a consistent comparison between processes of different nature, the space is normalised using the sensitivity indicator described in the previous section. Fig. 28 shows an example of the resulting envelopes in the normalised space, with the two generic biases previously mentioned, from which the associated residual error levels can be retrieved by inverting the normalisation factor.

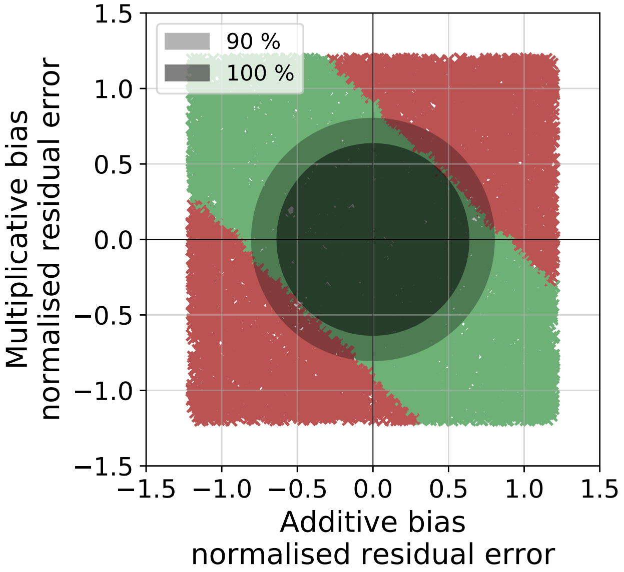

Figure 28: ESRA compliance domains for a combination of two generic biases

Since the random draws of residual error levels are currently following uniform distributions, the Monte-Carlo simulation is not necessary, and the radius of the 100% compliance domain (noted $r_{100\%}$ hereafter) can be determined analytically. The distributions should eventually be adjusted, so that the constraints related to each bias are taken into account and the explored domain can be more representative of the instrument. This approach will be introduced in the following section. In the normalised space, the size of these domains is indeed independent from the simulation scenarios, channels or ESRA levels, as this parameters are taken into account in the normalisation factor. The radius of the domains then only depends on the number of biases (n) and the chosen ESRA margin (m). $\delta x_{100\%}$ is considered as the normalised residual error for which the maximal ESRA level, corresponding to the required budget limited by the margin, is reached.

$$ESRA(\delta x_{100\%}) = ESRA_{max} = ESRA_{required} \cdot (1 - m)$$

This case occurs when there are no compensation between biases' effects. The corresponding ESRA is then the sum of all contributions:

$$ESRA(\delta x_{100\%}) = \sum_{n} s_n \cdot \delta x_{100\%} = n \cdot ESRA_{required} \cdot \delta x_{100\%}$$

where s_n is the normalisation of the proportionality coefficient between the ESRA and the residual error level, which is determined with the gain matrices and corresponds to $\frac{ESRA_{required}}{\delta x_0}$. After normalisation, δx_0 is equal to 1, and s_n is equal to $ESRA_{required}$. As the different bias considered here are assumed to be independent, they should be summed quadratically (Pythagorean sum), and thus the resulting domain is a hypersphere of dimension n. The radius of the compliance domain can be determined using $\delta x_{100\%}$, with $r_{100\%} = \sqrt{n} \cdot \delta x_{100\%}$, the analytical expression of the radius is consequently:

$$r_{100\%} = \frac{1 - m}{\sqrt{n}}$$

Two ways to consider a margin for the allocations of ESRA envelopes are therefore possible, either by lowering the global ESRA budget with the m parameter or by increasing the number of yet unknown biases.

Considering six biases, the 100% domain is then achieved for 36% of the maximal allowable residual error, while the radius of the 90% compliance domain corresponds to 78%. The corresponding allowable residual error levels obtained for each of these biases are summarised in Table 3. As they depend on the normalisation factor, which vary according to simulation case, channel or ESRA level, the most constraining values is retained.

Radiance factor biases		Residual error levels	
		90% compliance	100% compliance
Additive	(-)	0.029	0.013
Multiplicative	(-)	0.025	0.011
Straylight	(-)	0.091	0.042
Contamination	(nm)	2.5	1.1
Solar variability	(-)	1	0.475
Polarisation	(-)	0.982	0.453

Table 3: Allowable residual error levels for the six identified biases

5.5.3. Discussion

The random draws of residual error combinations are currently following uniform distributions within the explored domains. These distributions should however be adjusted so that the residual error levels are more representative of the instrumental constraints. For instance, gaussian functions of small variance could be considered to concentrate the draws around lower levels of residual errors. As a result, the 90% compliance domain would be extended, since the resulting scattering of the sampled biases would make combinations of higher residual error levels less likely, and would then allow to relax constraints for other biases. The 100% domain would however be less impacted by this different distribution, as it depends on the worst case in term of biases compensations and is inferred from the number of biases. It would then be broaden if the biases' distributions are asymmetrical, which corresponds to a negligible contribution of a bias in the quadratic sum. Fig. 29 shows the new domains for the polarisation and contamination-induced biases using arbitrarily chosen gaussians with respectively 0.07 and 0.6 standard deviations, leading to a 10% increase of the 100% compliance domain radius.

Examples of distributions that could be considered for a combination of the six biases are plotted in Fig. 30. In this theoretical case, the 90% compliance domain radius would reach 95.7% of the maximal allowable error, instead of the 78% that were obtained using only uniform distributions. These bias distributions are to be refined as the instrument's behaviour will be better assessed and modeled, and according to the correction strategies that will be foreseen for each specific bias source.

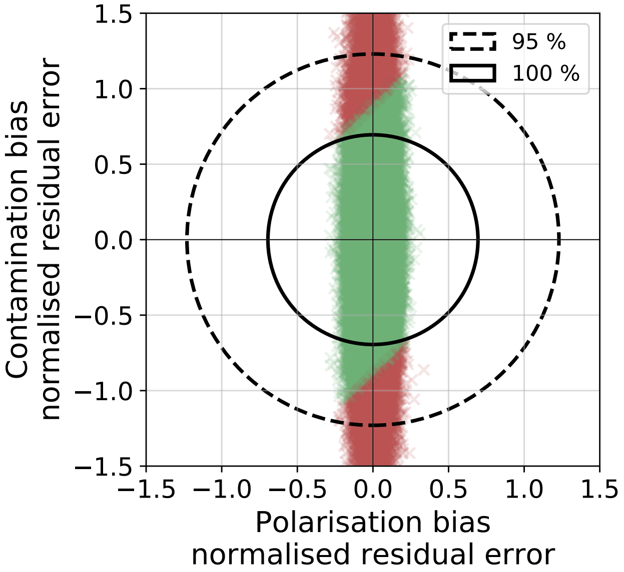

Figure 29: Example of ESRA compliance domains for a combination of the polarisation-induced and contamination-induced biases

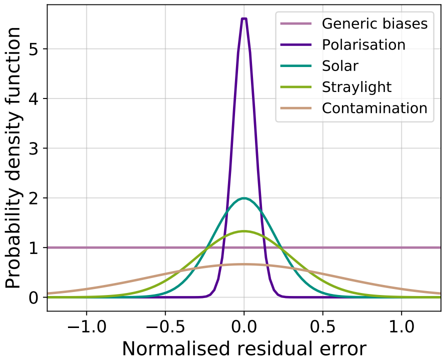

Figure 30: Examples of probability density functions for the Monte-Carlo simulation, for the six identified biases

6. Conclusion

The UV spectrometer VenSpec-U onboard ESA's EnVision mission will perform observations of Venus' upper atmosphere, focusing on the sulphured gases and dynamical properties. After reviewing its scientific objectives and the instrumental concept, as well as reminding the main requirements regarding the retrievals accuracy, the approaches implemented for the random and systematic errors management were presented. Both studies rely on the Radiative Transfer Model that allows to convert a set atmospheric parameters into radiance factor spectra and inversely. This model has been developed for the data analysis of SPICAV/Venus-Express and has been adjusted to match VenSpec-U's targeted wavelength ranges.

First, the impact of random errors on the uncertainties associated to the atmospheric parameters derived from the inverse RTM have been studied. The aim was to investigate how the Signal-to-Noise Ratio could be altered while maintaining acceptable precisions and comply with the specifications that were defined to reach the scientific goals. It was then shown that the required precisions are achieved in most cases, and new less constraining SNR boundaries have been estimated.

Secondly, the approach implemented for the characterisation of the systematic errors' effects on the accuracy of the retrievals was introduced. This accuracy is estimated with the ESRA requirement and involves a gain matrices formalism, which allows to use a common method to treat independently the various sources of biases that could be encountered by the instrument during the mission. Two ways of computing these gain matrices using the Radiative Transfer Model, both in the direct and inverse form, were detailed. The method that could be adopted to allocate residual error levels for each biases was then presented. Contributions of multiple biases and their potential compensations were also studied, regarding the compliance rate with respect to the specifications. The presented results are however preliminary and will need to be refined in the future when instrumental knowledge has progressed and bias removal algorithms been defined, so that an updated study using the method introduced here will be more representative of the actual instrument. Moreover, even if the present study is specific to VenSpec-U, the formalism we used is more general in scope, and could be applied to other any spectral or imaging instrument as long as gain matrices can be computed from a (linearised) forward model.

References

Barker, E.S., 1979. Detection of SO_2 in the *UV* spectrum of Venus. Geophysical Research Letters 6, 117–120. doi:10.1029/GL006i002p00117.

Bogumil, K., Orphal, J., Homann, T., Voigt, S., Spietz, P., Fleischmann, O.C., Vogel, A., Hartmann, M., Kromminga, H., Bovensmann, H., Frerick, J., Burrows, J.P., 2003. Measurements of molecular absorption spectra with the SCIAMACHY pre-flight model: instrument characterization and reference data for atmospheric remote-sensing in the 230–2380 nm region. Journal of Photochemistry and Photobiology A: Chemistry 157, 167–184. doi:10.1016/S1010-6030(03)00062-5.

Bolsée, D., Pereira, N., Gillotay, D., Pandey, P., Cessateur, G., Foujols, T., Bekki, S., Hauchecorne, A., Meftah, M., Damé, L., Hersé, M., Michel, A., Jacobs, C., Sela, A., 2017. SOLAR/SOLSPEC mission on ISS: In-flight performance for SSI measurements in the UV. Astronomy & Astrophysics 600, A21. doi:10.1051/0004-6361/201628234. publisher: EDP Sciences.

Copernicus Sentinels 4 & 5 MRTD, ESA, 2017. COPERNICUS SENTINELS 4 AND 5 MISSION REQUIREMENTS TRACEABILITY DOCUMENT. Technical Report. ESA.

Esposito, L.W., 1984. Sulfur Dioxide: Episodic Injection Shows Evidence for Active Venus Volcanism. Science 223, 1072–1074. doi:10.1126/science.223.4640.1072. publisher: American Association for the Advancement of Science.

Esposito, L.W., Copley, M., Eckert, R., Gates, L., Stewart, A.I.F., Worden, H., 1988. Sulfur dioxide at the Venus cloud tops, 1978 - 1986. Journal of Geophysical Research 93, 5267–5276. doi:10.1029/JD093iD05p05267. aDS Bibcode: 1988JGR....93.5267E.

Esposito, L.W., Winick, J.R., Stewart, A.I., 1979. Sulfur dioxide in the Venus atmosphere: Distribution and implications. Geophysical Research Letters 6, 601–604. doi:10.1029/GL006i007p00601. aDS Bibcode: 1979GeoRL...6..601E.

Garvin, J., Getty, S., Arney, G., Johnson, N., Kohler, E., Schwer, K., Sekerak, M., Bartels, A., Saylor, R., Elliott, V., Goodloe, C., Garrison, M., Cottini, V., Izenberg, N., Lorenz, R., Malespin, C., Ravine, M., Webster, C., Atkinson, D., Zolotov, M., 2022. Revealing the Mysteries of Venus: The DAVINCI Mission. The Planetary Science Journal 3. doi:10.3847/PSJ/ac63c2.

Ghail, R., Wilson, C.F., Widemann, T., Bruzzone, L., Dumoulin, C., Helbert, J., Herrick, R., Marcq, E., Mason, P., Rosenblatt, P., Vandaele, A., Burtz, L., 2017. EnVision: understanding why our most Earth-like neighbour is so different. arXiv: Earth and Planetary Astrophysics .

Head, J.W., Campbell, D.B., Elachi, C., Guest, J.E., McKenzie, D.P., Saunders, R.S., Schaber, G.G., Schubert, G., 1991. Venus Volcanism: Initial Analysis from Magellan Data. Science 252, 276–288. doi:10.1126/science.252.5003.276. publisher: American Association for the Advancement of Science.

Heays, A.N., Stark, G., Lyons, J.R., de Oliveira, N., Lewis, B.R., Gibson, S.T., 2023. Ultraviolet photoabsorption in the $B^3\Sigma^- - X^3\Sigma^-$ and $C^3\Pi - X^3\Sigma^-$ band systems of SO sulphur isotopologues. Molecular Physics 121, e2153092. URL: `https://doi.org/10.1080/00268976.2022.2153092`, doi:10.1080/00268976.2022.2153092. publisher: Taylor & Francis _eprint: https://doi.org/10.1080/00268976.2022.2153092.

Helbert, J., Vandaele, A.C., Marcq, E., Robert, S., Ryan, C., Guignan, G., Rosas-Ortiz, Y.M., Neefs, E., Thomas, I.R., Arnold, G., Peter, G., Widemann, T., Lara, L.M., 2019. The VenSpec suite on the ESA EnVision mission to Venus, in: Strojnik, M., Arnold, G.E. (Eds.), Infrared Remote Sensing and Instrumentation XXVII, SPIE, San Diego, United States. p. 6. doi:10.1117/12.2529248.

Heyden, F.J., Kiess, C.C., Kiess, H.K., 1959. Spectrum of Venus in the Violet and Near-Ultraviolet. Science (New York, N.Y.) 130, 1195. doi:10.1126/science.130.3383.1195.

Jessup, K.L., Marcq, E., Mills, F., Mahieux, A., Limaye, S., Wilson, C., Allen, M., Bertaux, J.L., Markiewicz, W., Roman, T., Vandaele, A.C., Wilquet, V., Yung, Y., 2015. Coordinated Hubble Space Telescope and Venus Express Observations of Venus' upper cloud deck. Icarus 258, 309. doi:10.1016/j.icarus.2015.05.027.

Lee, Y.J., Muñoz, A.G., Yamazaki, A., Quémerais, E., Mottola, S., Hellmich, S., Granzer, T., Bergond, G., Roth, M., Gallego-Cano, E., Chaufray, J.Y., Robidel, R., Murakami, G., Masunaga, K., Kaplan, M., Erece, O., Hueso, R., Kabáth, P., Špoková, M., Sánchez-Lavega, A., Kim, M.J., Mangano, V., Jessup, K.L., Widemann, T., Sugiyama, K.i., Watanabe, S., Yamada, M., Satoh, T., Nakamura, M., Imai, M., Cabrera, J., 2022. Reflectivity of Venus's Dayside Disk During the 2020 Observation Campaign: Outcomes and Future Perspectives. The Planetary Science Journal 3, 209. doi:10.3847/PSJ/ac84d1. publisher: IOP Publishing.

Luginin, M., Fedorova, A., Belyaev, D., Montmessin, F., Wilquet, V., Korablev, O., Bertaux, J.L., Vandaele, A.C., 2016. Study of aerosol properties in the upper haze of Venus from SPICAV IR data .

Marcq, E., Baggio, L., Lefèvre, F., Stolzenbach, A., Montmessin, F., Belyaev, D., Korablev, O., Bertaux, J.L., 2019. Discovery of cloud top ozone on Venus. Icarus 319, 491–498. doi:10.1016/j.icarus.2018.10.006.

Marcq, E., Bertaux, J.L., Montmessin, F., Belyaev, D., 2013. Variations of sulfur dioxide at the cloud top of Venus's dynamic atmosphere. Nature Geoscience advance online publication. doi:10.1038/ngeo1650.

Marcq, E., Lea Jessup, K., Baggio, L., Encrenaz, T., Lee, Y.J., Montmessin, F., Belyaev, D., Korablev, O., Bertaux, J.L., 2020. Climatology of SO_2 and UV absorber at Venus' cloud top from SPICAV-UV nadir dataset. Icarus 335, 113368. doi:10.1016/j.icarus.2019.07.002.

Marcq, E., Mills, F.P., Parkinson, C.D., Vandaele, A.C., 2018. Composition and Chemistry of the Neutral Atmosphere of Venus. Space Science Reviews 214, 10. doi:10.1007/s11214-017-0438-5. aDS Bibcode: 2018SSRv..214...10M.

Marcq, E., Montmessin, F., Lasue, J., Bézard, B., Jessup, K.L., Lee, Y.J., Wilson, C.F., Lustrement, B., Rouanet, N., Guignan, G., 2021. Instrumental requirements for the study of Venus' cloud top using the UV imaging spectrometer VeSUV. Advances in Space Research 68, 275–291. doi:10.1016/j.asr.2021.03.012.

Markiewicz, W.J., Titov, D.V., Ignatiev, N., Keller, H.U., Crisp, D., Limaye, S.S., Jaumann, R., Moissl, R., Thomas, N., Esposito, L., Watanabe, S., Fiethe, B., Behnke, T., Szemerey, I., Michalik, H., Perplies, H., Wedemeier, M., Sebastian, I., Boogaerts, W., Hviid, S.F., Dierker, C., Osterloh, B., Böker, W., Koch, M., Michaelis, H., Belyaev, D., Dannenberg, A., Tschimmel, M., Russo, P., Roatsch, T., Matz, K.D., 2007. Venus Monitoring Camera for Venus Express. Planetary and Space Science 55, 1701–1711. doi:10.1016/j.pss.2007.01.004.

Mcclintock, W., Rottman, G., Woods, T., 2000. Solar Stellar Irradiance Comparison Experiment II (SOLSTICE II) for the NASA Earth Observing System's Solar Radiation and Climate Experiment mission. Proceedings of SPIE - The International Society for Optical Engineering 4135. doi:10.1117/12.494220.

Meftah, M., Sarkissian, A., Keckhut, P., Hauchecorne, A., 2023. The SOLAR-HRS New High-Resolution Solar Spectra for Disk-Integrated, Disk-Center, and Intermediate Cases. Remote Sensing 15, 3560. doi:10.3390/rs15143560. number: 14 Publisher: Multidisciplinary Digital Publishing Institute.

Mills, F.P., Allen, M., 2007. A review of selected issues concerning the chemistry in Venus' middle atmosphere. Planetary and Space Science 55, 1729–1740. doi:10.1016/j.pss.2007.01.012.

Moroz, V.I., Zasova, L.V., 1997. VIRA-2: A review of inputs for updating The Venus International Reference Atmosphere. Advances in Space Research 19, 1191–1201. doi:10.1016/S0273-1177(97)00270-6.

Muscari, J.A., 1980. Nonmetallic materials contamination studies, final technical report .

Na, C.Y., Esposito, L.W., Skinner, T.E., 1990. International ultraviolet explorer observation of Venus SO_2 and SO. Journal of Geophysical Research: Atmospheres 95, 7485–7491. doi:10.1029/JD095iD06p07485. _eprint: https://onlinelibrary.wiley.com/doi/pdf/10.1029/JD095iD06p07485.

Newville, M., Otten, R., Nelson, A., Ingargiola, A., Stensitzki, T., Allan, D., Fox, A., Carter, F., Michał, Pustakhod, D., Ram, Y., Glenn, Deil, C., Stuermer, Beelen, A., Frost, O., Zobrist, N., Mark, Pasquevich, G., Hansen, A.L.R., Spillane, T., Caldwell, S., Polloreno, A., andrewhannum, Fraine, J., deep 42-thought, Maier, B.F., Gamari, B., Persaud, A., Almarza, A., 2020. lmfit/lmfit-py 1.0.1. doi:10.5281/zenodo.3814709.

Peralta, J., Hueso, R., Sánchez-Lavega, A., Piccioni, G., Lanciano, O., Drossart, P., 2008. Characterization of mesoscale gravity waves in the upper and lower clouds of Venus from VEX-VIRTIS images. Journal of Geophysical Research: Planets 113, 2008JE003185. doi:10.1029/2008JE003185.

Piccialli, A., Titov, D.V., Sanchez-Lavega, A., Peralta, J., Shalygina, O., Markiewicz, W.J., Svedhem, H., 2014. High latitude gravity waves at the Venus cloud tops as observed by the Venus Monitoring Camera on board Venus Express. Icarus 227, 94–111. doi:10.1016/j.icarus.2013.09.012.

Pérez-Hoyos, S., Sánchez-Lavega, A., García-Muñoz, A., Irwin, P.G.J., Peralta, J., Holsclaw, G., McClintock, W.M., Sanz-Requena, J.F., 2018. Venus Upper Clouds and the UV Absorber From MESSENGER/MASCS Observations. Journal of Geophysical Research: Planets 123, 145–162. doi:10.1002/2017JE005406. _eprint: https://onlinelibrary.wiley.com/doi/pdf/10.1002/2017JE005406.

Sierk, B., Bézy, J.L., Meijer, Y., Jurado, P., Caron, J., Löscher, A., 2014. The CarbonSat candidate mission for imaging greenhouse gases from space: concepts and system requirements, p. 94. doi:10.1117/12.2304154.

Smrekar, S., Hensley, S., Dyar, D., Whitten, J., Nunes, D., Helbert, J., Iess, L., Mazarico, E., 2022. VERITAS (Venus Emissivity, Radio Science, Insar, To-pography And Spectroscopy): A Selected Discovery Mission 44, 339. Conference Name: 44th COSPAR Scientific Assembly. Held 16-24 July ADS Bibcode: 2022cosp...44..339S.

Stamnes, K., Tsay, S.C., Wiscombe, W., Jayaweera, K., 1988. Numerically stable algorithm for discrete-ordinate-method radiative transfer in multiple scattering and emitting layered media. Applied Optics 27, 2502–2509. doi:10.1364/AO.27.002502. publisher: Optica Publishing Group.

Titov, D., Taylor, F., Svedhem, H., Ignatiev, N., Markiewicz, W., Piccioni, G., Drossart, P., 2008. Atmospheric structure and dynamics as the cause of ultraviolet markings in the clouds of Venus. Nature 456, 620–3. doi:10.1038/nature07466.

Titov, D.V., Markiewicz, W.J., Ignatiev, N.I., Song, L., Limaye, S.S., Sanchez-Lavega, A., Hesemann, J., Almeida, M., Roatsch, T., Matz, K.D., Scholten, F., Crisp, D., Esposito, L.W., Hviid, S.F., Jaumann, R., Keller, H.U., Moissl, R., 2012. Morphology of the cloud tops as observed by the Venus Express Monitoring Camera. Icarus 217, 682–701. doi:10.1016/j.icarus.2011.06.020.

Vandaele, A.C., Korablev, O., Belyaev, D., Chamberlain, S., Evdokimova, D., Encrenaz, T., Esposito, L., Jessup, K.L., Lefèvre, F., Limaye, S., Mahieux, A., Marcq, E., Mills, F.P., Montmessin, F., Parkinson, C.D., Robert, S., Roman, T., Sandor, B., Stolzenbach, A., Wilson, C., Wilquet, V., 2017. Sulfur dioxide in the Venus atmosphere: I. Vertical distribution and variability. Icarus 295, 16–33. doi:10.1016/j.icarus.2017.05.003.

Widemann, T., Smrekar, S., Garvin, J., Straume, A., Ocampo, A., Schulte, M., Voirin, T., Hensley, S., Dyar, M., Whitten, J., Nunes, D., Getty, S., Arney, G., Johnson, N., Kohler, E., Spohn, T., O'Rourke, J., Wilson, C., Way, M., Desai, N., 2023. Venus Evolution Through Time: Key Science Questions, Selected Mission Concepts and Future Investigations. Space Science Reviews 219. doi:10.1007/s11214-023-00992-w.

Yamazaki, A., Yamada, M., Lee, Y.J., Watanabe, S., Horinouchi, T., Murakami, S.y., Kouyama, T., Ogohara, K., Imamura, T., Sato, T., Yamamoto, Y., Fukuhara, T., Ando, H., Sugiyama, K.i., Takagi, S., Kashimura, H., Ohtsuki, S., Hirata, N., Hashimoto, G., Nakamura, M., 2018. Ultraviolet imager on Venus orbiter Akatsuki and its initial results. Earth, Planets and Space 70. doi:10.1186/s40623-017-0772-6.

Zhang, X., Liang, M.C., Mills, F.P., Belyaev, D.A., Yung, Y.L., 2012. Sulfur chemistry in the middle atmosphere of Venus. Icarus 217, 714–739. doi:10.1016/j.icarus.2011.06.016.